SANDIA REPORT SAND86-8010 • Unlimited Release • UC-62a
Printed October 1986

Testing of the Molten Salt Electric Experiment Solar Central Receiver in an External Configuration

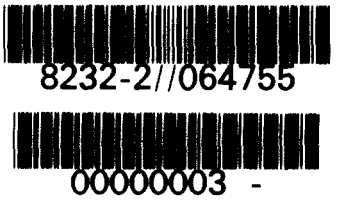

N. E. Bergan

Prepared by
Sandia National Laboratories
Albuquerque, New Mexico 87185 and Livermore, California 94550
for the United States Department of Energy
under Contract DE-AC04-76DP00789

Issued by Sandia National Laboratories, operated for the United States Department of Energy by Sandia Corporation.

Printed in the United States of America
Available from
National Technical Information Service
5285 Port Royal Road
Springfield, VA 22161

NTIS price codes
Printed copy: A05
Microfiche copy: A01

UC-62a

SAND 86-8010
Unlimited Release
Printed October 1986

TESTING OF THE MOLTEN SALT ELECTRIC EXPERIMENT SOLAR CENTRAL RECEIVER IN AN EXTERNAL CONFIGURATION

Nina E. Bergan
Solar Central Receiver Division
Sandia National Laboratories, Livermore

ABSTRACT

The cavity surrounding the Molten Salt Electric Experiment (MSEE) solar central receiver was removed and the receiver was tested in an external configuration to compare external and cavity performance. The thermal efficiency of the external receiver was slightly less than that of the cavity receiver. However, operationally, the external receiver was easier to start up. Convective losses were measured from the external receiver and compared to analytical correlations. Measured convective losses were found to be 10% to 100% lower than predictions, most likely due to correction factors used in the predictions to account for surface roughness and wind direction.

Four demonstration tests were performed on the external receiver. A high flux test exposed the receiver to flux levels of $1MW/m^2$. The receiver was successfully filled in a serpentine rather than the customary flood pattern; and in another test the receiver was filled at temperatures below the freezing point of salt (470 ° F). In the final demonstration test, hot salt was used to keep the receiver warm overnight to allow sunrise start up. Receiver thermal losses overnight exceeded energy saved by reduced parasitics and energy collected from the sunrise start up, making overnight conditioning uneconomical for this receiver.

SOLAR THERMAL TECHNOLOGY

Foreword

The research and development described in this document was conducted within the U.S. Department of Energy's (DOE) Solar Thermal Technology Program. The goal of the Solar Thermal Technology Program is to advance the engineering and scientific understanding of solar thermal technology, and to establish the technology base from which private industry can develop solar thermal power production options for introduction into the competitive energy market.

Solar thermal technology concentrates solar radiation by means of tracking mirrors or lenses onto a receiver where the solar energy is absorbed as heat and converted into electricity or incorporated into products as process heat. The two primary solar thermal technologies, central receivers and distributed receivers, employ various point and line-focus optics to concentrate sunlight. Current central receiver systems use fields of heliostats (two-axis tracking mirrors) to focus the sun's radiant energy onto a single tower-mounted receiver. Parabolic dishes up to 17 meters in diameter track the sun in two axes and use mirrors or Fresnel lenses to focus radiant energy onto a receiver. Troughs and bowls are line-focus tracking reflectors that concentrate sunlight onto receiver tubes along their focal lines. Concentrating collector modules can be used alone or in a multi-module system. The concentrated radiant energy absorbed by the solar thermal receiver is transported to the conversion process by a circulating working fluid. Receiver temperatures range from 100 ° C in low-temperature troughs to over 1500 ° C in dish and central receiver systems.

The Solar Thermal Technology Program is directing efforts to advance and improve promising system concepts through the research and development of solar thermal materials, components, and subsystems, and the testing and performance evaluation of subsystems and systems. These efforts are carried out through the technical direction of DOE and its network of national laboratories who work with private industry. Together they have established a comprehensive, goal directed program to improve performance and provide technically proven options for eventual incorporation into the Nation's energy supply.

To be successful in contributing to an adequate national energy supply at reasonable cost, solar thermal energy must eventually be economically competitive with a variety of other energy sources. Components and system-level performance targets have been developed as quantitative program goals. The performance targets are used in planning research and development activities, measuring progress, assessing alternative technology options, and making optimal component developments. These targets will be pursued vigorously to insure a successful program.

The work presented in this report was performed as part of the Central Receiver Systems task and examines the performance of an external molten salt central receiver. The results of this study will be used to assist the work performed in the Systems Studies task of the Solar Central Receiver Program.

Acknowledgements

Many people contributed to the experiment described in this report. In particular, I would like to acknowledge and thank the following people: Dan Barron and Stan Saloff from McDonnell Douglas Astronautics Company, as test engineers at the CRTF; Tibor Buna from Solar Power Engineering Company, for heliostat aiming strategies and thermal/hydraulic analysis; Professor R. Boehm and H. Nakhaie from University of Utah, for convective loss data analysis and interpretation; and, Prof. Larryl Matthews from New Mexico State University, for cavity wall temperature measurements and analysis.

CONTENTS

ILLUSTRATIONS

TABLES

TESTING OF THE MOLTEN SALT ELECTRIC EXPERIMENT SOLAR CENTRAL RECEIVER IN AN EXTERNAL CONFIGURATION

Section 1. Executive Summary

The Molten Salt Electric Experiment External Receiver Test Program was conducted at the Central Receiver Test Facility in Albuquerque, New Mexico from May to July 1985. During this time the MSEE (Molten Salt Electric Experiment) receiver was tested in both a cavity and an external (billboard) configuration.

All four objectives of the MSEE External Test Program were met: 1) external receiver operation was demonstrated, 2) cavity versus external comparison tests were performed, 3) optimized external performance tests were completed, and 4) convective loss tests were run. In addition, four demonstration tests were performed. These included a high flux test, a serpentine receiver fill, a cold receiver fill, and an overnight conditioning test using hot salt.

Cavity versus External Comparison Tests

The cavity-to-external receiver performance showed that, for this receiver, the point-in-time thermal efficiency of the cavity receiver is 9% ±5% higher than the external receiver. Calculations indicate that most of the difference is due to larger radiation losses for the exposed, external receiver configuration.

Operational differences between the two receivers were also observed. The external receiver was easier to warm up, resulting in a shorter start-up time; however, during extended cloud cover a cavity receiver would be kept operational (running in cold flow) longer than an external configuration.

The impact of the thermal performance differences and operational characteristics on annual performance cannot be quantified directly from MSEE data. Annual performance for different receiver configurations is being addressed in the Systems Improvement Studies at Sandia National Laboratories in Livermore [Falcone, 1986]. Data from both the MSEE Power Production Campaign [Holl et al., 1986] and External Receiver Tests are being used in these annual performance models.

The cavity-to-external comparative test used a heliostat aiming strategy designed to minimize spillage in the cavity. In order to accomplish this, only 80% of the heliostat field was used for the cavity and the external comparative tests. This resulted in approximately 4 MW_{th} total power to the receiver, with a design-point peak flux of 0.6 MW/m^2 at the absorber panel.

Optimized External Receiver Tests

The objective of the optimized external receiver test was to provide performance data for the external receiver using the full, 5 MW_{th} heliostat field. Data indicate that the measured efficiency using an "optimized" aimpoint strategy for the external configuration is not significantly different from the measured efficiency using an aimpoint designed to give a flux pattern similar to the cavity receiver and does not vary over the incident power levels measured. Even so, the "optimized" data is limited by the hardware in this experiment. In the external configuration, the MSEE absorber panel is too large for the 5 MW_{th} field, and the allowed design flux is only generated for a portion of the receiver surface. This results in relatively larger thermal losses than would be expected for a receiver which operates with the allowable flux over most of the surface.

Convective Losses

Convective losses were measured for the external receiver using both "flux-off" and "flux-on" techniques. Data from the MSEE receiver shows that measured convective losses are lower than analytical predictions for combined forced and natural convection. General trends in the predictive techniques are mirrored in the experimental data, despite high experimental uncertainties. Comparisons of predicted heat transfer coefficients and experimental data indicate that predictions are almost always higher than data. Much of the discrepancy is due to correction factors in the correlation for surface roughness and wind direction. The effect of convective losses from the MSEE receiver on receiver thermal efficiency is evaluated. The receiver efficiency is calculated during high and low wind conditions using analytical correlations for forced and natural convections. As wind speeds increase from zero to thirty miles per hour, receiver efficiency decreases by 2% to 8%, depending on the correction factors used in the forced convection correlation. This calculation shows the importance of the forced convection correlation on thermal efficiency calculations. The degree to which measured convective losses agree with analytical predictions is important because the predictions are used in computer models to calculate full-scale receiver thermal performance. These models are part of central receiver systems optimization studies ongoing at Sandia National Laboratories Livermore. A report describing convective losses from the MSEE receiver in detail is published separately by Prof. R. Boehm, University of Utah [Boehm et al., 1986].

Demonstration Tests

The demonstration tests showed the feasibility of several receiver design options. First, the high flux test showed that the receiver survived 1.0 MW/m^2 for over one hour with no apparent damage. This was the first time a molten salt receiver had been exposed to flux levels over 0.75 MW/m^2, and it demonstrated that peak fluxes higher than the MSEE design level of 0.60 MW/m^2 may be possible for future receivers. Higher peak fluxes will result in higher average fluxes and therefore higher thermal efficiencies.

Second, a serpentine fill experiment was successfully performed. There was no indication of trapped air in any of the tubes, although it is possible that small amounts of air may have been undetected in the headers. The receiver was operated normally following the serpentine fill. Potential effects of trapped air in the receiver resulting from serpentine fill need to be evaluated in future experiments. However, this test demonstrated the feasibility of filling the receiver without the use of purge valves at the top of each header. Eliminating purge valves would result in a cleaner and less expensive receiver design as well as a simpler start-up procedure.

Third, the receiver "cold fill" experiment was also successful. In this test, 700 ° F salt was introduced into a receiver with temperatures below the melting point of salt. No problems were encountered until the the panel temperature was below 210 ° F. At this point, some salt blockage occurred in the receiver tubes. Further experiments will be necessary to characterize the phenomenon. The ability to fill a receiver below the freezing point of salt (470 ° F) would allow for much greater operational flexibility: the receiver could be filled earlier in the warm-up sequence, and clear sky conditions are not required.

Finally, the overnight conditioning test showed that flowing salt through the external receiver overnight is feasible but involves large thermal losses from the salt. Overnight conditioning with salt has been considered as an alternative to keeping the receiver pipes and valves warm with electrical trace heating. The benefits of overnight conditioning include reduced energy requirements from trace heating and sunrise start-up. Benefits of overnight conditioning do not outweigh the thermal losses in the MSEE external receiver. A trade study for larger receivers must be conducted to determine the economics for commercial-scale plants.

Related Analytical Studies

Two additional studies related to the MSEE were carried out concurrently with the experiment: the measurement and calculation of cavity wall temperatures and the development of heliostat aiming strategies used in this testing.

Cavity wall temperatures were measured by placing thermocouples 1/8 to 1/4 inch below the surface of the insulation. The highest temperature read from the receiver thermocouples was 600 ° F. A computer program which models the heat transfer within the insulation duplicated this observation. The model predicts insulation temperatures between 500 ° F and 700 ° F, with the peak temperature approximately 1/8 inch below the surface.

Six different heliostat aiming strategies were used during the External Receiver Test Program. These aiming strategies were determined using a computer program called DOMAIN which employs a double-projection mapping technique, coupled with HELIOS, a program to calculate flux levels on the receiver. The determination of the desired aiming strategies was accomplished using the program THERMOFLUID to calculate salt and metal temperatures.

These two studies are documented in Appendices C and D to this report.

Section 2. Introduction

The MSEE External Receiver Test Program was the final phase of the Molten Salt Electric Experiment. A brief description of the Central Receiver Test Facility, in Albuquerque, New Mexico, is included in Section 3 of this report. Further details can be found in [Holl, et al., 1986] and [Martin Marietta Corp. 1985]. Figure 1 shows an aerial view of the Central Receiver Test Facility.

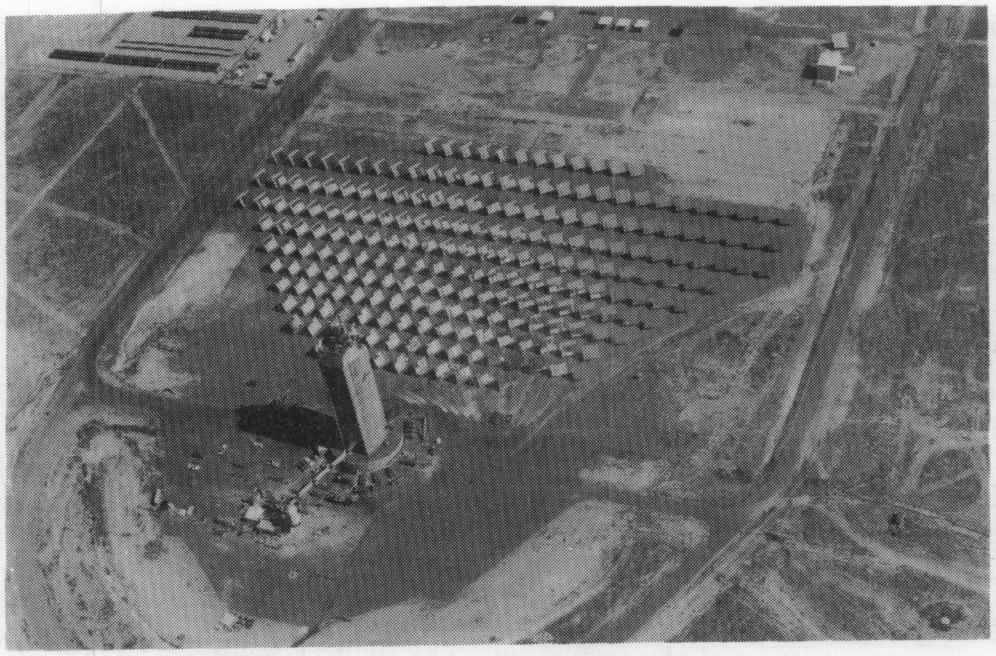

Figure 1. Aerial view of Central Receiver Test Facility in Albuquerque, New Mexico

The External Receiver Test Program was conducted during the time between the end of the Power Production Phase of MSEE and the start of the next receiver project, the Molten Salt Subsystem/Component Experiment Test: from May 13, 1985, to July 26, 1985. Figure 2 shows the test schedule.

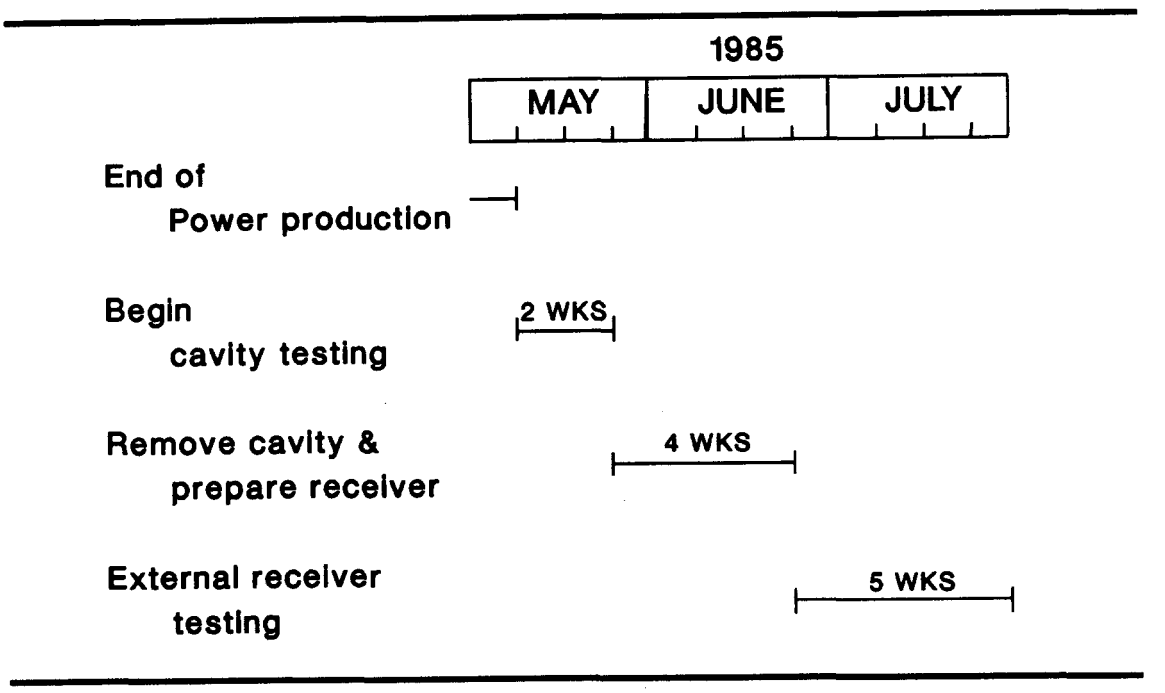

Figure 2. The MSEE External Receiver Test Program schedule

The four objectives of the MSEE External Receiver Test Program were to:

1. demonstrate operation of external molten salt receiver,

2. compare performance of external and cavity MSEE receivers — both operational and thermal performance,

3. provide performance data for the MSEE external receiver (thermal efficiency data), and

4. measure convective losses of MSEE external receiver and compare this data to analytical predictions.

Section 3. MSEE System Description

The Molten Salt Electric Experiment was conducted at the Central Receiver Test Facility in Albuquerque, New Mexico.

The MSEE converts solar energy to electricity using molten nitrate salt (60% $NaNO_3$, 40% KNO_3) as the energy collection and storage medium. The energy stored in the molten salt is transferred to water and steam to generate electricity with a conventional Rankine steam cycle turbine generator. The receiver, located at the top of the CRTF tower, receives concentrated solar energy from the collector field. Figure 1 shows an aerial view of the Central Receiver Test Facility with the Molten Salt Electric Experiment Cavity Receiver on top of the tower; Figure 3 shows a system schematic; and Figure 6 shows the MSEE receiver as tested in an external configuration.

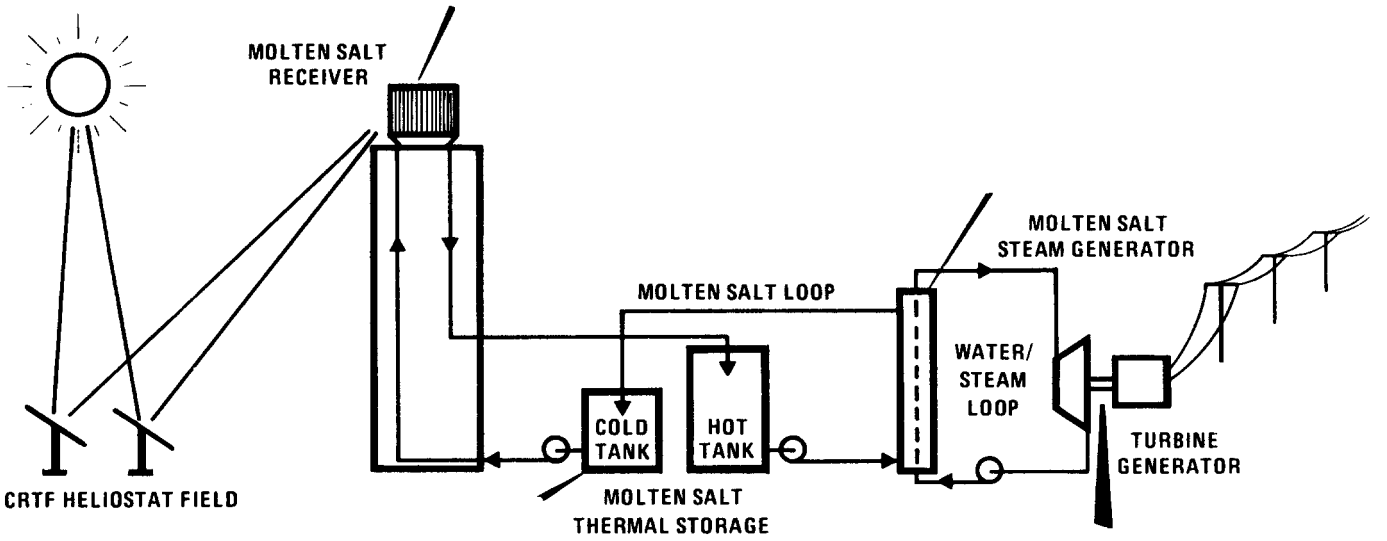

Figure 3. Molten Salt Electric Experiment System Schematic

Molten salt from the "cold" (570 ° F) storage tank, located at ground level, is circulated through the receiver and heated to 1050 ° F. Salt then flows through the downcomer, into the hot salt storage tank. Hot salt from storage is pumped through

the steam generator superheater and evaporator and returned to the cold storage tank. Main steam from the steam generator drives a conventional steam turbine-generator. The electricity generated is supplied into a utility grid network. (The turbine-generator was not operated during the MSEE external test program.) The MSEE system is divided into the following subsystems:

The Collector Subsystem redirects, concentrates, and focuses solar radiation onto the tower-mounted receiver. This subsystem consists of 221 two-axis tracking heliostats (211 used for MSEE) located north of the receiver tower. Under optimum insolation and heliostat conditions, the heliostat field can concentrate approximately 5.5 megawatts of thermal energy onto the receiver.

The Receiver Subsystem, located at the top of the CRTF tower, intercepts and absorbs concentrated energy from the heliostat field and transfers this energy to the molten salt. The cavity receiver subsystem consists of the receiver absorber panel, cavity enclosure with a vertical aperture door, insulation, heat tracing, cold surge tank, booster pump, hot surge tank, overflow tank, instrumentation, and control valves.

The Thermal Storage Subsystem decouples the energy collection process from the energy conversion process. It provides a cold (570 ° F) salt supply source for the receiver and a hot (1050 ° F) salt supply source for the steam generator; it absorbs or supplies the differences in their flow demands. Because the thermal storage capacity is 7 MW-hours thermal there is some capacity for "resource shifting." This subsystem includes the hot and cold salt storage tanks, propane-fired salt heater (to allow for experimental flexibility), cold salt pump, and cold salt sump.

The Steam Generation Subsystem transfers heat from the molten salt to produce superheated steam for the turbine-generator. This subsystem includes an evaporator, steam drum, boiler water recirculation pump, superheater, attemperator, and the hot salt pump.

The Electric Power Generation Subsystem was not used during this part of the MSEE program. Details of the turbine generator operation can be found in [Holl, et al., 1986].

The Heat Rejection and Feedwater Subsystem rejects waste heat to the atmosphere, and pressurizes, heats and deaerates the condensate to the final feedwater conditions. This subsystem includes six air cooling towers, circulating water pump, deaerator, spray water heat exchanger, spray water pump, feedwater pump, feedwater heater, demineralizers, chemical feeders, water analyzers, and condensate makeup pump.

The Master Control Subsystem consists of an Emcon-D2 for primary system control. A Bailey Network 90 system is used to directly control the Steam Generation Subsystem. The Network 90 operation and control functions are directed from the EMCON console through a hardwired interface. Additionally, an Acurex Data Logger collects and displays all the temperature measurements relating to the

heat tracing and data instrumentation. The Logger also performs certain logical control functions, such as activation of heat trace circuitry and generation of go/no-go signals for the EMCON system. The data acquisition system utilizes both the EMCON-D2 and the Hewlett-Packard HP-1000. The EMCON system collects the data, and the HP-1000 system stores and displays data.

The Equipment Protection Subsystems is an independent hardwired relay system using dedicated sensors. It is designed to shut down safely the MSEE in the event of any potentially unsafe condition. The relay units are independent of the EMCON and the Network 90 control systems.

In addition to the project report by McDonnell Douglas, Delameter, et al, [1986] has written a report summarizing the overall accomplishments and key issues of the Molten Salt Electric Experiment.

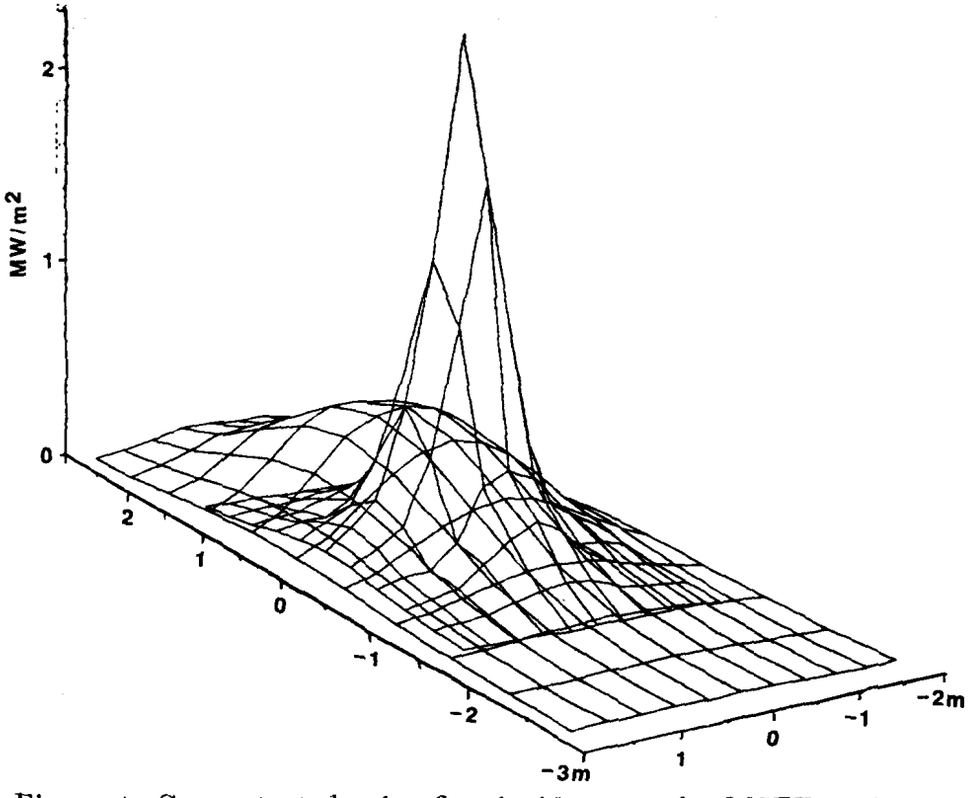

Figure 4. Concentrated solar flux incident on the MSEE cavity aperture and absorber panel

SECTION 4. INCIDENT SOLAR FLUX

Calculations

The solar flux incident on the receiver is important for thermal efficiency calculations and comparisons. Unlike the other data from this experiment, solar flux

incident on the MSEE receiver was not measured during this test period. A computer code, HELIOS, was used to calculate the flux distribution on the receiver, the flux missing the receiver target (spillage), and the total power on the receiver. HELIOS calculates flux density and total power on a target given insolation, time of year, time of day, a complete description of the heliostat field (including prealignment points), and a geometrical description of the target. Figure 4 shows the results of a HELIOS calculation of the flux distribution on the MSEE cavity aperture and absorber panel. The heliostat beams are concentrated in the plane of the aperture, and diverge as they approach the absorber panel, resulting in a more uniform flux distribution on the absorber panel.

A complete description of the HELIOS computer code and its accuracy can be found in [Maxwell, et al., 1985] and [Vittitoe, et al., 1981]. Possible differences between HELIOS predictions and the actual flux on the receiver are due to several assumptions within the code. First, HELIOS assumes a specific error band around each ray as it traces that ray from the heliostat to the target. This error band may cause inaccuracies in heliostat tracking calculations, getting worse as the day progresses. Currently HELIOS has no mechanism to account for this time of day problem. In addition, HELIOS assumes each heliostat tracks the sun perfectly, when actually each heliostat has its own bias in the form of a hardware/software parameter. Finally, at the time of the MSEE external testing, a heliostat alignment procedure had updated the alignment of only 181 out of 211 heliostats. This condition results in some overprediction of the actual total power on the receiver.

HELIOS's high relative accuracy was used to minimize the uncertainty in the incident power calculation for the cavity and the external receiver. First, the cavity aimpoint was optimized to minimize internal spillage. This resulted in a HELIOS total power prediction (for day 143) as shown in Figure 5. The external comparative aimpoint was chosen to be as similar as possible to the cavity comparative aimpoint. The heliostat aiming strategy, the total power and the peak flux are approximately the same. The resulting aimpoint is described in Appendix C, and the HELIOS prediction of total power as a function of time of day (for day 177) is shown in Figure 5. The relative accuracy of the incident power is assumed to be within $\pm 5\%$.

Heliostat Aiming Strategies

Six different heliostat aiming strategies were developed for the External Receiver Test. The details of the algorithm used to determine the aiming strategies are given in Appendix C of this report, published in Volume 2. Table I lists the total power and peak flux predictions from HELIOS for each of the six aimpoints at solar noon on representative test days.

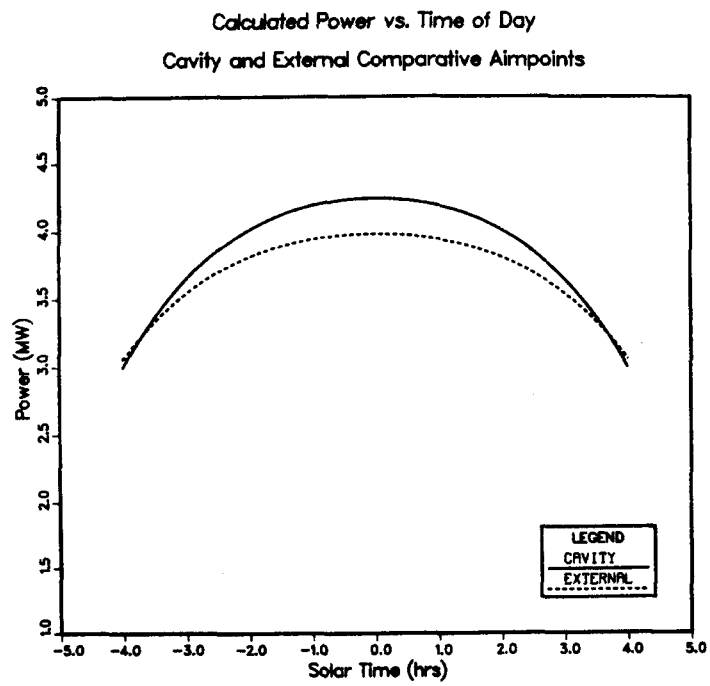

Figure 5. HELIOS prediction for total power to receiver as a function of time of day for the Cavity Comparative Aimpoint, Day 143 and External Comparative Aimpoint, Day 177. Peak flux at solar noon is 0.6 MW/m^2 for both aimpoints

Table I
HELIOSTAT AIMING STRATEGIES USED DURING THE EXTERNAL RECEIVER TEST

Aimpoint	Total Power (MW)	Peak Flux (MW/m^2)
(1.) Comparative cavity	4.0	0.6
(2.) Comparative external	4.0	0.6
(3.) Optimized external	5.0	0.6
(4.) Barron's flux-on convective loss test (2 aimpoints)	3.6/1.8	0.6/0.3
(5.) Early A.M. optimized external	3.0	0.4
(6.) High flux external	5.0	1.0

Spillage

For a cavity receiver, the thermal efficiency is defined in terms of incident power through the aperture. Therefore, flux incident on uncooled portions of the cavity

(internal spillage) is not absorbed by the working fluid and therefore degrades the thermal efficiency of a cavity receiver.

External spillage is a related phenomena. For both a cavity and an external receiver, external spillage is the flux which misses the aperture or absorber panel target, respectively. External spillage will degrade the system efficiency in that available solar energy is spilled onto non-absorbing surfaces; but the receiver thermal efficiency will not be affected by external spillage.

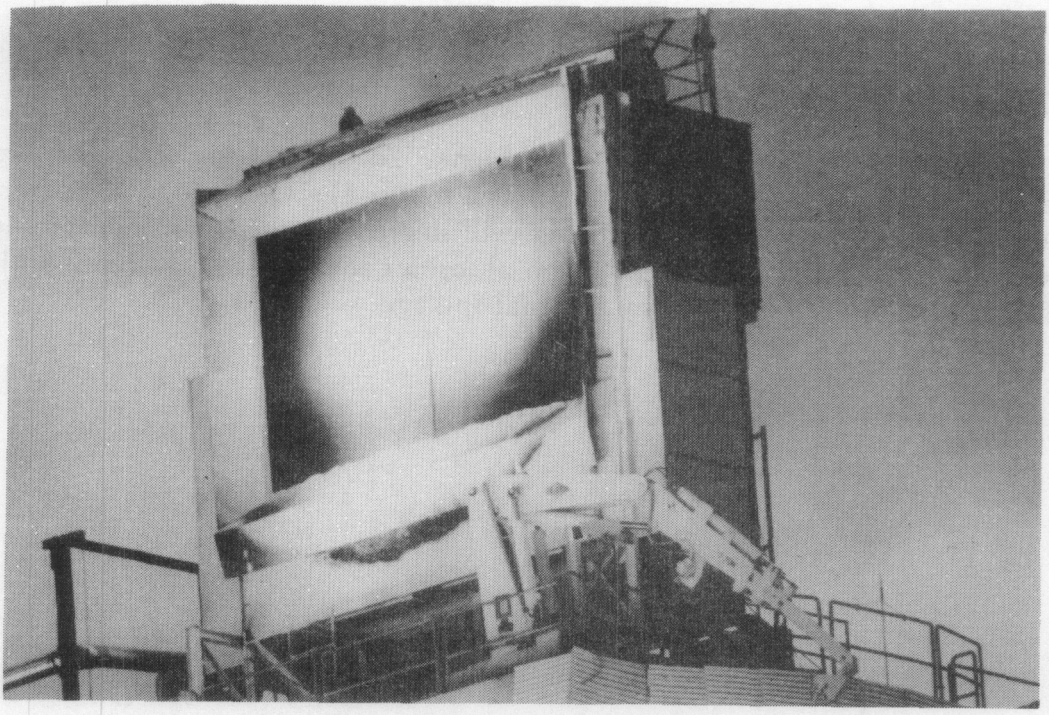

Figure 6. The MSEE receiver as tested in an external configuration

Section 5. Results of Engineering Tests

The four objectives of the test program as stated in Section 2 were accomplished using four basic groups of tests: (1) Checkout, (2) Cavity vs. External Comparison Tests, (3) Optimized External Performance Tests, and (4) Convective Loss Tests.

Test 1) Checkout — During checkout, operation of the external molten salt receiver was verified. Originally there was some concern that the receiver losses would be too great to operate in high wind conditions. The receiver operated without problems in all weather conditions encountered in this test program. Based on our experience, we do not foresee any weather conditions which would constitute a risk of freezing the salt.

Test 2) Cavity to External Comparison Tests — Our comparison of cavity and external receivers includes thermal and operational performance issues. Since MSEE cavity operational performance was already established during the past year of testing, this test program needed only to determine operational performance for the external receiver. For thermal performance comparisons, however, the original cavity aimpoint had an unrealistically high value of internal spillage (around 14%) and made previous efficiency data biased against the cavity configuration. Therefore, prior to removing the cavity from the MSEE receiver, two weeks of cavity testing was performed using a new, "comparative" cavity aimpoint which reduced

internal spillage and allowed a fairer comparison between the cavity and external configuration.

Thermal Performance, Efficiency

The point-in-time thermal efficiency of a central receiver is defined to be the power absorbed by the receiver working fluid divided by the power incident on the receiver. For a cavity receiver the incident power is that power which comes through the cavity aperture. For an external receiver, incident power is that incident on the absorber panel. Internal and external spillage is the incident power which misses the receiver absorber panel. Section 4 of this report described these terms in more detail.

It is important to distinguish between point-in-time thermal efficiency and daily or annual efficiency. In order to evaluate a receiver design in terms of busbar energy costs, the annual thermal efficiency of the receiver must be determined. This quantity can be calculated either by integrating the absorbed and incident power over the year and then dividing them, or by integrating the divided quantities over the year. The relative merits of these methods are discussed in [Sayers 1985]. In any case, point-in-time thermal performance comparisons can be quite different from daily or annual performance comparisons, depending on operational characteristics. By itself, data from the MSEE External Receiver Test Program cannot be extrapolated to annual performance. Rather the data from this experiment provided a reference point for ongoing analytical receiver optimization studies.

Two heliostat aiming strategies were developed in order to compare the thermal efficiency of the cavity and the external receivers: a cavity comparative aimpoint and an external comparative aimpoint. By reducing internal spillage, the cavity comparative aimpoint improved the thermal efficiency of the cavity receiver. This allowed for a fairer comparison to the external receiver, which would not be affected by spillage. Parameters from the original cavity aimpoint are compared to the comparative cavity aimpoint in Table 2. In order to reduce internal spillage from 15% to 4%, the total power was derated to 4 MW.

TABLE II
COMPARISON OF ORIGINAL AND COMPARATIVE CAVITY AIMPOINTS

Quantity	Original Aimpoint	Comparative Aimpoint
Internal spillage	15%	4%
External spillage	14%	16%
Total power	5 MW	4 MW
Peak flux	0.6 MW/m^2	0.6 MW/m^2
H'stats on target	211	182

The cavity comparative aimpoint sets the constraints for the external comparative aimpoint. The most accurate efficiency comparison is made if the incident power to the cavity and external receivers are the same for both aimpoints. * Due to the geometry of the incoming flux rays, the total power and flux distribution is never exactly the same, but major differences are avoided. HELIOS predictions for total power incident on the receiver for the cavity and external comparative aimpoints as a function of time of day are shown in Figure 5. These predictions are made for representative days in the test period of each configuration assuming 950 W/m^2 insolation and do not account for inoperational heliostats. Corrections are subsequently made for each of these phenomena as necessary. Details are given in Appendix B.

Data from the MSEE receivers show the point-in-time cavity thermal efficiency to be marginally higher than external thermal efficiency. The thermal losses from the cavity receiver are approximately 250 kW less than for the external receiver. This difference amounts to 35% of the losses from the external receiver. All data is for winds less than 5 mph. At approximately the same power level, the thermal efficiency of the cavity receiver is roughly 9% higher than the point-in-time thermal efficiency of the external receiver. Figure 7 shows receiver thermal efficiency for both receivers plotted as a function of time of day. The thermal efficiency comparison is most accurate when made at the same time of day and approximately the same incident total power. However, as Figure 7 shows, the thermal efficiency does not vary significantly over the range of incident powers experienced during this test. The difference in thermal performance between the cavity and the external receiver is close to experimental accuracy. The error bounds do overlap, although the data indicates that the cavity receiver is more efficient than the external receiver.

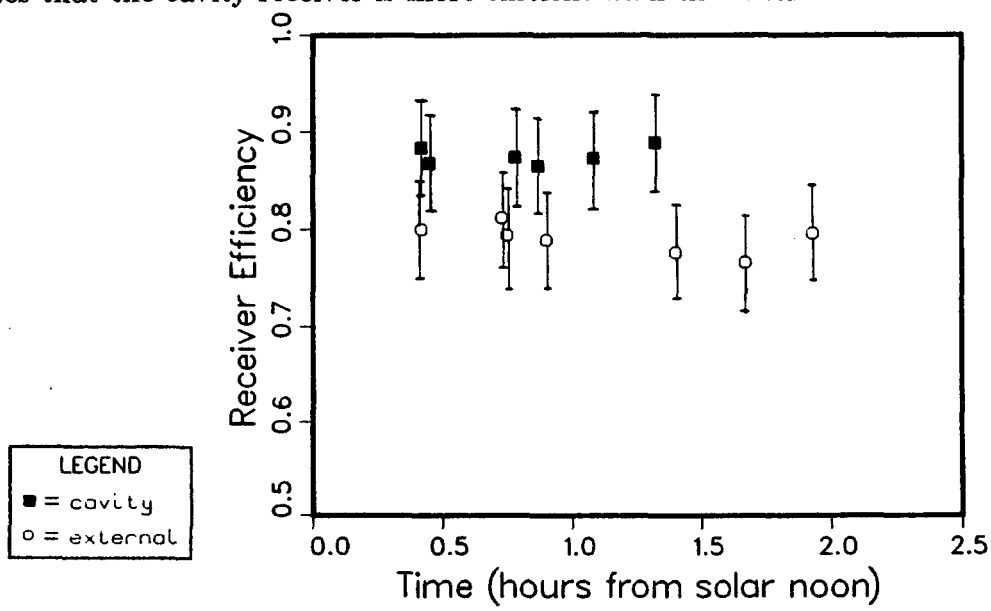

Figure 7. Receiver thermal efficiency for cavity and external configurations versus time of day

* Details provided in Appendix A.

Operational Performance

Because the MSEE cavity receiver had been operating since May 1984, sufficient operational data existed for the cavity receiver before the start of this test program. Early morning start-up with the cavity receiver was accomplished within 60 minutes of the actual sunrise. *

In the external configuration, the receiver was easier to start up. The heliostat warming pattern was more uniform and easier to control, and the start-up time was 5 minutes less than for the cavity. Further refinement of the heliostat warming strategy could reduce warm-up times even more.

Shut down of the receiver involves defocusing the heliostats, opening the purge and drain valves, and draining the receiver. There was no difference in the shut down procedure between the cavity and the external receiver.

Initially, cloud transients were thought to be a possible threat to the operation of an external molten salt receiver. Two problems exist in operating a central receiver through cloud transients. One deals with short cloud transients and is a function of the control algorithm's ability to anticipate the sun's return. The other problem deals with long cloud transients and is a function of the thermal losses from the receiver.

Response to short cloud transients is actually more a function of the receiver control algorithm than of the receiver itself. The external receiver responded to short cloud transients (approximately 1 to 30 minutes) the same as the cavity receiver. The MSEE control algorithm was not able to adequately compensate for a sudden return of the sun; in which case the set point was depressed from 1050 ° F to 900 ° F to avoid overshooting the outlet temperature when the sun returned.

Longer cloud transients (>30 minutes) are an important issue when comparing receiver geometries. Longer cloud transients can cause two problems. First, if receiver thermal losses are excessive, the risk of freezing the salt during cold flow operation is greater (i.e. flowing 550 ° F to 600 ° F salt through the receiver with no incident flux). Secondly, extended cloud cover can be uneconomical to "wait out" if thermal losses from the receiver are excessive. The economics of this energy trade-off can be calculated for any receiver, the thermal losses are known.

Ideally, it is desirable to operate a receiver through extended cloud cover anticipating return of the sun, so that the receiver is ready to collect whatever energy is available. The energy trade-off comes in not losing more energy in cold flow than is collected when the sun returns. Thus, minimizing thermal losses from the receiver maximizes the receiver's worth in long cloud transient conditions.

The size of the MSEE absorber panel is larger than optimum. Although the

* Note: due to mountains located on the eastern horizon, the sun actually rose 16 minutes *after* theoretical sunrise. In this report, all times are referenced to actual sunrise.

MSEE receiver was designed to be tested as an external and a cavity receiver, the resulting design is not optimized for 5 MW_t. Recent studies [Dawson, 1986] have shown external absorber areas as much as 25% smaller are appropriate for external and cavity receivers of the same thermal rating. The larger panel size means thermal losses from the MSEE receiver are higher than would be expected from an optimum design. Therefore operational optimizations are not meaningful for this receiver.

In summary, the external receiver was easier to warm-up, allowed a more uniform flux distribution across the receiver, but experienced higher thermal losses than the cavity receiver. In order to optimize daily system efficiency, these higher thermal losses would necessitate shutting down the external receiver earlier than the cavity receiver during extended cloud cover, resulting in a penalty on annual performance.

Test 3) Optimized External Performance Tests — The objective of the optimized external receiver test was to provide performance data for the external receiver using the full, 5 MW_{th} heliostat field. An optimized external aimpoint was developed which kept the peak flux at its design point, 0.6 MW/m^2, using all 211 heliostats.

Data indicate that the measured "optimized" external efficiency is not significantly different from the external "comparative" aimpoint. Even so, the "optimized" performance is limited by the hardware in this experiment. In the external configuration, the MSEE absorber panel is too large for the 5 MW_{th} field. This results in increased thermal losses and lower average fluxes on the receiver than would exist if the absorber area were smaller. Figure 8 shows the optimized external efficiency plotted as a function of full power of incident on the receiver. For the data obtained during the test, the optimized external receiver efficiency does not vary significantly with incident power. Comparing Figures 7 and 8 we see that the optimized external receiver efficiency is not significantly different than that with the comparative external aimpoint.

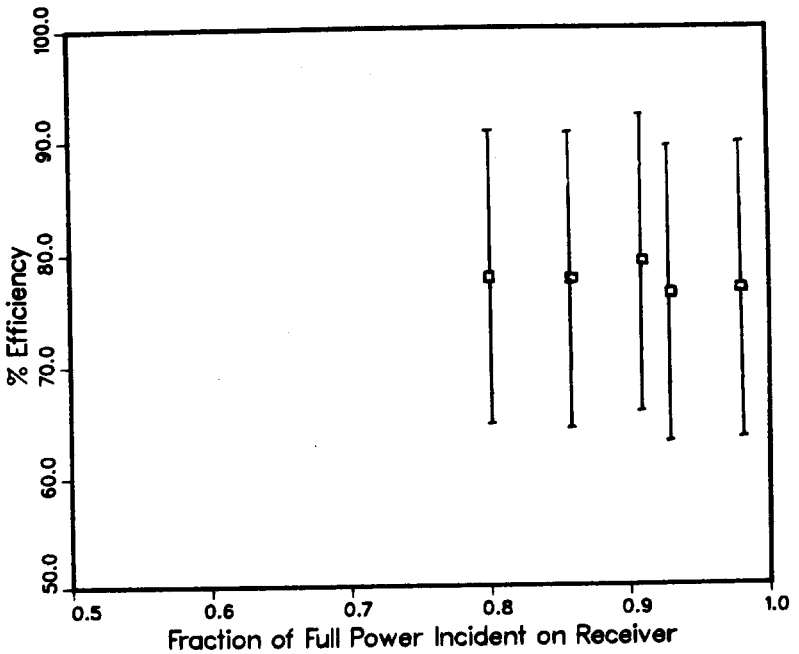

Figure 8. Optimized external receiver efficiency as a function of full power incident on the receiver

Test 4) Convective Loss Tests—Convective losses were measured for the external receiver using both "flux-off" and "flux-on" techniques. Flux-off measurements are made with salt flowing through the receiver and with no solar flux. Thermal losses are then determined by measuring the temperature drop of the salt across the receiver.

Flux-on measurements are made using two different methods: one developed by Martin Marietta Engineers (Buna's method) and one developed by McDonnell Douglas Engineers (Barron's method). Both methods eliminate incident power (an unknown quantity) from the calculations. In Buna's method, measurements are taken at two different receiver temperatures under nearly constant incident flux. In Barron's method, measurements are taken at two different levels of incident flux and assume receiver temperature is constant. Barron's two levels of incident flux are achieved by first using 100% of the aligned heliostats and then 50%. In both flux-on methods the absorbed power is calculated from the flow rate and temperature rise of the salt. With the assumption of either constant incident flux (Buna's method) or constant receiver temperature (Barron's method), total thermal losses are deduced from the two measurements of absorbed power. For both the flux-off and flux-on measurement techniques, radiation losses are determined analytically and subtracted from the total thermal losses, leaving convective losses.

Buna's method of flux-on loss testing was not successful on the MSEE external receiver. This method is not sensitive enough to detect convective losses under

experimental conditions encountered in this test.

Barron's method of flux-on loss testing, however, yielded three data points, two of which appear to be valid. The third data point produced total losses less than expected radiative losses — an impossible condition. It appears that this third data point was not taken at steady-state.

By far the largest amount of data was generated from flux-off loss testing. A cold flow, flux-off loss test can be performed in much less time than a flux-on test. In addition, each flux-off loss test results in many data points, while flux-on loss tests give only one data point per test.

Comparison of Experimental Data to Correlations

Data from thermal loss tests were reduced using the method described in [Boehm, et. al, 1986]. Measured convective heat transfer coefficients are used to validate empirical correlations for convective losses. Despite high experimental uncertainties, we find predictive correlations which mirror the general trends in the experimental data. However, in almost all cases, flux-off thermal loss data from the MSEE external receiver shows that measured convective losses are lower than predictions for combined forced and natural convection.

Figure 9 shows measured mixed convective heat transfer coefficients plotted against the corresponding predicted values. Predictions are derived from empirical correlations for natural and forced convection from a cylinder suggested by Siebers and Kraabel [1984]. There are two differences between the correlations used here and those proposed by Siebers and Kraabel. First, a forced convection correction factor to account for wind direction was added. The forced convention correlation for wind parallel to a smooth flat plate multiplied by a factor two to account for wind perpendicular to the receiver. Thus,

$$h_{\perp} = 2h_{\parallel}$$

Angles between zero and ninety degrees are interpolated using a simple trigometric function. Second, the surface roughness factor, $\pi/2$, suggested by Seibers and Kraabel was included in the correlations for both forced and smooth convection. This factor was later removed to examine its effect.

The baseline empirical correlations used to compare against data are, for natural convection:

$$Nu_n = (\frac{\pi}{2})0.098Gr^{1/3}(T_r/T_i nf)^{-0.14}$$

and for forced convection for wind parallel to the receiver plane:

$$Nu_f = (\frac{\pi}{2})0.0287 Re_{0.8} Pr_{1/3}$$

where Nusselt number, Nu is defined to be the heat transfer coefficient, h, times the appropriate distance along the receiver (the width, W, for forced convection, and the length, L, for natural covection), times the thermal condutivity of air, k. Thus,

$$h_n = Nu_n k/L$$

and the forced convection heat transfer coefficient is:

$$h_f = Nu_f k/W$$

Forced and natural convective heat transfer coefficients are added as suggested by Siebers and Kraabel to form a single convective heat transfer coefficient for the system:

$$h_c = (h_f^3.2 + h_n^3.2)^{1/3.2}$$

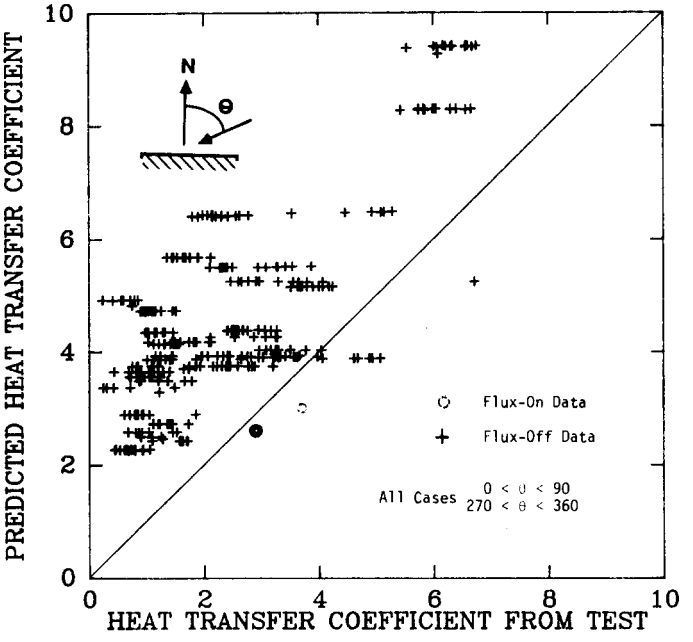

Figure 9. Measured vs. predicted convective heat transfer coeffficients. Flux-on and flux-off tests. Wind is from all directions. Predictions include $\pi/2$ surface roughness factor for forced and natural convection, and wind direction correction factor of 2, i.e., $h_\perp = 2h_\parallel$. Correlations overpredict heat transfer coefficients by 10% to 100%

Figure 9 shows that the adjusted correlations overpredict heat transfer coefficients by 10% to 100%. This discrepancy is most likely due to correction factors for surface roughness and wind direction. Further perturbations on correction factors, trying to match experimental data with analytical correlations, can be found in [Boehm, et al, 1986]. The conclusion from the MSEE data is that the $\pi/2$ surface roughness factor should be removed from both the natural and forced convection correlation. Figure 10 shows the same data as in Figure 9, this time with no $\pi/2$ correction factor in the prediction for forced and natural convection. The correction for wind direction, $h_{\perp} = 2h_{\parallel}$, was changed to a factor of 1.5 in Figure 11. This causes the larger convective heat transfer coefficients to match the experimental data, indicating that the correction for wind direction may need to be a function of the magnitude of the heat transfer coefficient. The MSEE data indicates a wind direction correction around 2, decreasing to 1.5 for larger heat transfer coefficients.

These findings are similar to convective loss data from Solar One, an external, cylindrical water/steam receiver. Stoddard, 1985 found experimental data matched predictions better if no surface roughness correction was included for natural convection.

Effect of Convective Losses on Thermal Efficiency

Correction factors of $\pi/2$ and 2 in convective heat transfer coefficients carry more meaning when related to the thermal efficiency of the receiver. Defining thermal efficiency to be,

$$\eta = \frac{Q_{abs}}{Q_{abs} + Q_{losses}}$$

where,

$$Q_{losses} = Q_{conv} + Q_{rad}$$

a sample problem is worked using real data for absorbed power, and radiation losses were calculated as shown in [Boehm, et al, 1986]. The receiver efficiency is calculated during high and low wind conditions using analytical correlations for forced and natural convections. Figure 12 shows the results of this calculation. As wind speeds increase from zero to thirty miles per hour, receiver efficiency decreases by 2% to 8%, depending on the correction factors used in the forced convection correlation.

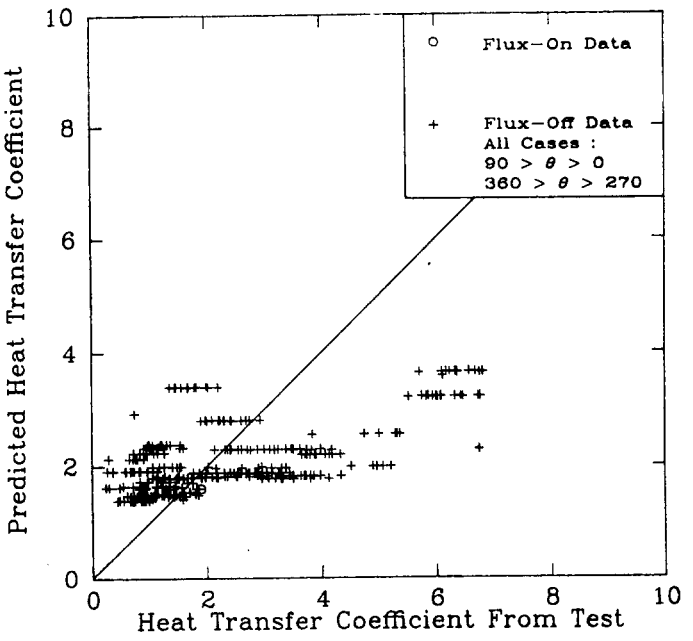

Figure 10. Measured vs. Predicted heat transfer coefficients. Same data as in Figure 9, except the predictions include no $\pi/2$ correction for natural or forced convection. Wind direction correction factor is 2, i.e., $h_{\perp} = 2h_{\parallel}$

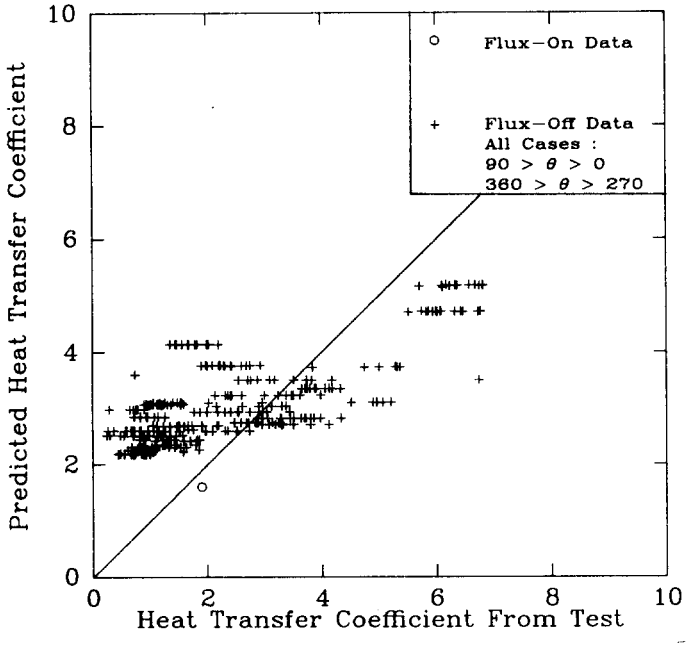

Figure 11. Same data as in Figure 9 except no $\pi/2$ correction for natural or forced convection, and wind direction correction factor is 1.5, i.e., $h_{\perp} = 1.5h_{\parallel}$

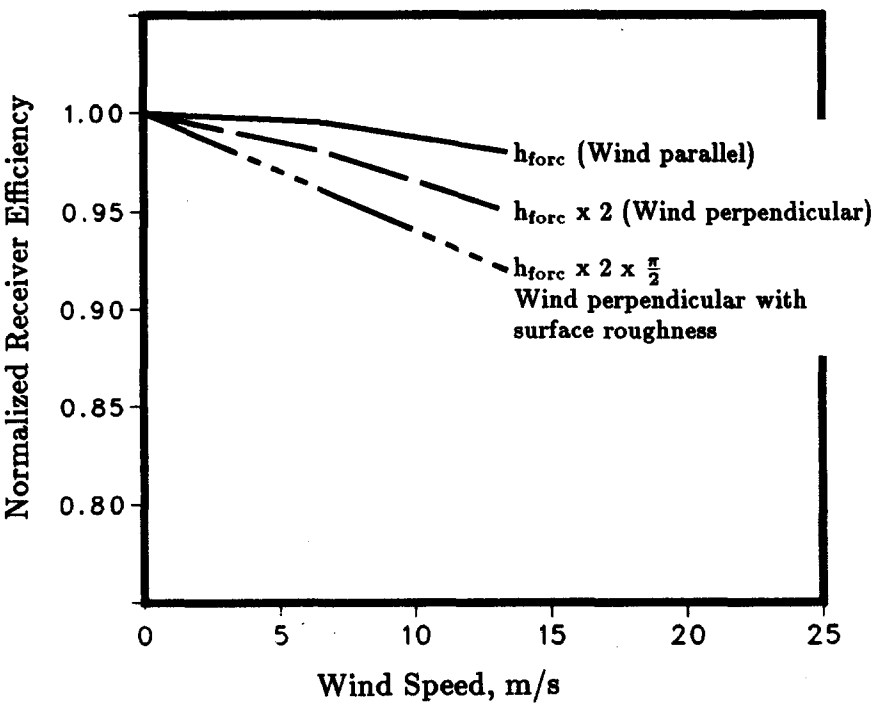

Figure 12. Calculated receiver thermal efficiency as a function of wind speed using three different sets of surface roughness and wind direction factors in the convective heat transfer coefficients

Section 6. Demonstration Test Results

Demonstration Test 1) Overnight Conditioning Test – In the overnight conditioning test, salt was circulated through the receiver loop overnight, using stored thermal energy in lieu of heliostats to keep the panel warm. At sunrise, the full heliostat field was aimed at the receiver.

In normal cold-start, the sun is used to pre-heat the receiver panel before salt is introduced. This is necessary because the receiver panel is not heat traced.

Objectives — The overnight conditioning test had four objectives.

1. Demonstrate thermal conditioning of the receiver loop using stored thermal energy rather than electric trace heaters.
2. Measure thermal energy required to keep the receiver panel warm overnight using flowing salt.
3. Collect maximum energy immediately after sunrise to determine the amount of collectable energy which is lost during the normal receiver start-up period.
4. Evaluate the economics of overnight conditioning and compare to standard operating procedures.

Test Results — High winds and heavy cloud cover occurred late in the evening of this test. The receiver losses more than doubled during periods of high winds. During the night, the clouds cleared and winds subsided, resulting in an ideal morning for performing the energy collection portion of the test.

The test began on July 7, 1985, at 6 p.m., which is approximately the time the receiver would normally be shut down, and continued until 7:30 the following morning. The overnight losses ranged from 120kW to almost 300kW; the higher losses corresponded to the periods of higher winds (up to 40 mph from the northeast). The sun rose over the mountains at 6:30 a.m. (16 minutes after theoretical sunrise).

Normally, a cold receiver warmed up using heliostats can be filled and operated at full power 60 minutes after sunrise: 7:30 a.m. for this day. Thus, the energy gained using overnight conditioning would be from 6:30 a.m. to 7:30 a.m.

The energy lost by the receiver from 6 p.m. until 6:30 a.m. the following day and the energy absorbed during the period of energy collection are shown in Table III.

TABLE III
ENERGY REQUIRED TO MAINTAIN RECEIVER OVERNIGHT
VERSUS ENERGY COLLECTED FROM SUNRISE START-UP

Test	Thermal Energy (KWh)	% of Clear Day Total
Receiver loss overnight (6:00 p.m. - 6:30 a.m.)	2010	7%
Collected from sunrise (6:30 a.m. - 7:30 a.m.)	190	0.6%

The above results show that there is no advantage to maintaining the MSEE external receiver warm overnight using flowing salt. Not enough energy can be collected in the morning to offset the expense of keeping the receiver warm. In fact, the receiver had to operate from 6:30 until 8:40 a.m. to recover the energy lost overnight.

In order to achieve an advantage over daily cold start-up the thermal losses would have to be reduced from 120kW to less than 15kW. For comparison, during testing of the receiver in the cavity configuration, the thermal losses during cold flow with the cavity door closed ranged from 20 to 40kW.

Conclusions — The receiver loop can be kept warm overnight using stored thermal energy. However, the collectable energy lost during cold start-up of the MSEE receiver is less than the energy required to maintain the receiver in a warm standby mode overnight, either with or without the cavity. Further discussions on the merits of overnight conditioning can be found in reference [9].

Demonstration Test 2) High Flux Test - A high flux heliostat aiming strategy was developed to produce 1 MW/m^2 flux on the receiver panel. This flux level was maintained for over an hour.

Objectives — The high flux test had two objectives:

1. Demonstrate successful operation of the receiver at 1 MW/m^2.
2. Compare thermal performance of receiver using high flux aimpoint and optimized external aimpoint.

Test Results — The high flux test was performed within one hour of solar noon, 12:02 to 1:14 p.m. At the conclusion of the high flux test, opertion continued using the optimized aimpoint.

Figure 13 shows results from a thermal/hydraulic computer code, using THERMOFLUD, which predicts 1130 ° F maximum I.D. temperature during the high flux test. Since corrosion from molten salt becomes significant at temperatures above 1150 ° F this would not be a desirable long-term operating point to provide a margin of safety.

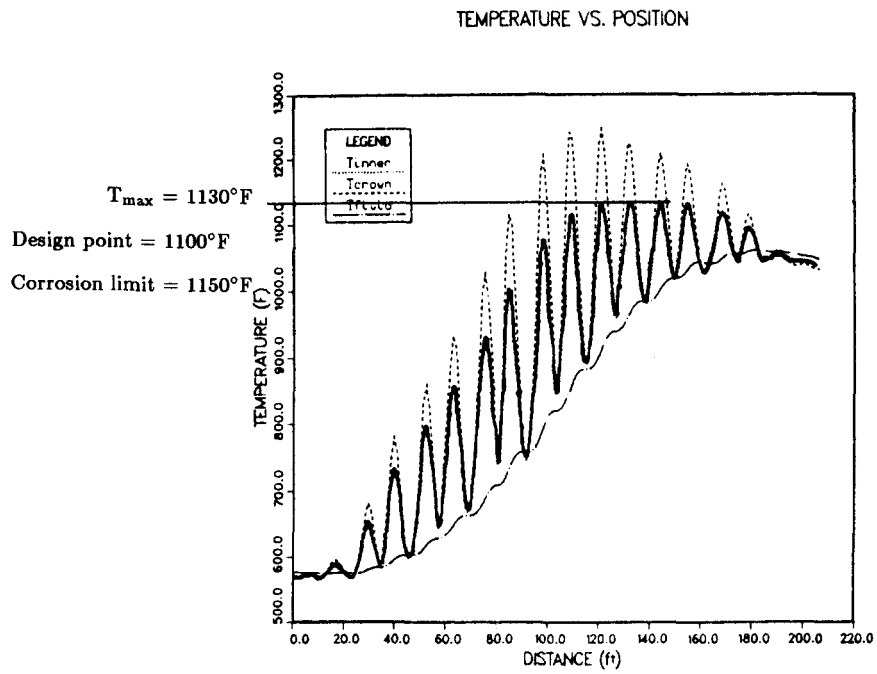

Figure 13. Computer code predictions of receiver temperature vs. flowpath distance

Thermal performance data from the MSEE receiver indicated a 2-3% increase in receiver output over the optimum aim point. Most likely this is due to reduced spillage. Visual inspection of the panel revealed no damage.

Conclusions — Limited, qualitative testing demonstrated that the MSEE receiver successfully operated at 1 MW/m^2 peak flux for a short duration. However, long term cyclic testing and data are required to draw conclusions about tube life. Recent studies by Kistler [1986] indicate that a conservative design peak flux for a molten salt receiver with Incoloy 800 tubes is 0.85 MW/m^2 incident, rather than the 0.6 MW/m^2. The advantage of a higher allowable peak flux is a smaller receiver, which reduces thermal losses thereby increasing the efficiency. A tradeoff, however, is higher spillage for the smaller receiver.

Demonstration Test 3) Receiver Serpentine Fill Test – The receiver panel was preheated using heliostats. All drain and purge valves were closed and the receiver was filled using only the riser, in a serpentine fill, rather than typical flood fill. All remaining heliostats were targeted back on the receiver to achieve full power output. Qualitative checks were made for air pockets in the headers. None were found.

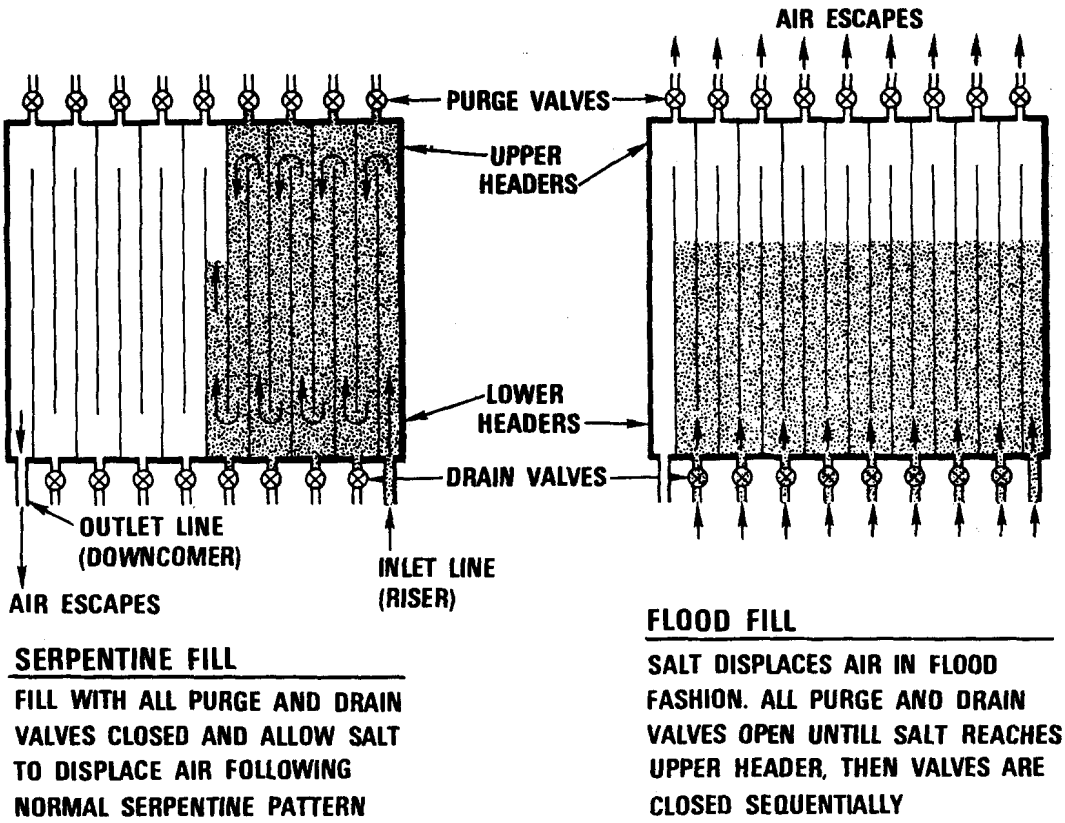

Figure 14. Two methods of filling a multipass central receiver: serpentine fill and flood fill

Objective — The objective of the serpentine fill test was to demonstrate filling the receiver without using the purge and drain valves.

Test Results — Using warm-up heliostats, the receiver panel was preheated to around 700 ° F. To achieve serpentine fill only, the riser was used to fill the receiver, with all purge and drain valves closed. After filling the receiver, full flow was verified by timing the depletion of the salt level in the cold sump. The purge valves were sequentially opened and closed to listen for air which might have been trapped in the upper headers. No unusual sounds were heard. The receiver was run at full power for thirty minutes with no complications.

Conclusions — Although this test alone is not quantitative proof, it appears that a receiver can be filled using serpentine flow from the riser without using purge and

drain valves. Using this method to fill the receiver would simplify the design and significantly reduce the cost by eliminating purge and drain valves. Note that at least one purge valve would still be necessary to create the siphon necessary to drain the receiver. Further study is required to verify the observations from this test.

Demonstration Test 4) Receiver Cold Fill Test — The nitrate salt used in the MSEE receiver begins to freeze at 474 ° F and is completely frozen at 432 ° F. Normally the receiver panel, which is the only part of the system not heat traced, is preheated to 500 ° F before salt is introduced. In this test the receiver was filled in its normal flood fashion, but with the absorber panel temperatures below the salt freezing point. The advantage of cold receiver fill lies in shorter start up times. Shorter start up times mean more energy can be collected in a day, and a long stretch of clear sky is not required to start the receiver. The latter is especially advantageous on partly cloudy days.

Objectives — The receiver cold fill test had three objectives:

1. Demonstrate filling of receiver panel at temperatures below the salt freezing temperature.

2. Demonstrate thawing of frozen panel using heliostats.

3. Determine minimum panel/salt temperatures at which the receiver can be successfully filled.

Test Results — This test was performed on the last day of the MSEE test program because of potential damage to the receiver. The receiver was filled and completely drained three times with different combinations of absorber panel and salt temperatures. The issue of thermal shock on the receiver tubes was not addressed.

After each filling operation, the relationship between receiver flow rate and inlet pressure was compared to the normal flow-vs.-pressure relationship to determine if partial blockage (individual tubes within a pass) existed. It was estimated that the flow rate and pressure measurement uncertainties would allow detection of five or more blocked tubes out of the total 288 tubes. However, if the salt freezes at all, chances are that it will freeze in a group of tubes, not just one. Therefore, this method is acceptable for determining a successful fill.

For the first cold fill, the minimum panel temperature was 325 ° F(approximately 105 ° F below the freezing point of salt) and the maximum panel temperature was 500 ° F. The temperature of the salt in the cold sump was increased from the nominal 570 ° F to 700 ° F prior to starting the fill sequence, by adding salt from the hot tank. This fill was successful with no apparent salt freezing.

For the second cold fill, the minimum panel temperature was reduced to 240 ° F and the salt temperature in the sump was reduced to 650 ° F. A more uniform temperature distribution on the panel was achieved for this test since the

absorber panel had been heated by the salt prior to draining after the first cold fill. The second cold fill was also successful.

For the third cold fill the minimum panel temperature was 212 ° F with 700 ° F salt in the sump. Under these conditions a partial blockage in the panel was observed. Before the purge and drain valves were closed, some of the back-tube thermocouples failed to respond to the molten salt temperatures. When the purge and drain valves were closed, a momentary spike in the receiver inlet pressure indicated there may have been a complete blockage in one or more passes which was cleared by the high pressure. Partial serpentine flow was established. Some blockage was evident since the inlet pressure was about 50% higher than normal for the given salt flow rate. Table IV summarizes these results.

TABLE IV
SUMMARY OF RESULTS OF COLD RECEIVER FILL TEST

Receiver Min. Temp. (°F)	Salt Temp. (°F)	Results
325	700	Fill O.K.
240	650	Fill O.K.
210	700	Partially frozen panel

To thaw the frozen salt, 15% of the heliostat field was targeted on the receiver. The salt flow rate, inlet pressure, and panel temperatures were carefully monitored during this operation. After approximately thirty minutes all thermocouples had returned to the molten salt temperature and the flow rate and pressure relationship were normal, indicating the blockage had been cleared. A visual inspection of the absorber panel revealed no obvious damage.

Conclusions — The MSEE receiver can be successfully filled with panel temperatures as much as 200 ° F below the salt freezing temperature (470 ° F) if the cold salt used for filling is at least 650 ° F. Further testing and analysis is required to determine other combinations of panel and salt temperatures which would be acceptable. If blockages occur, the receiver can be successfully thawed using a uniform, low power flux distribution on the absorber panel. However, the effects of thermal shock, both on filling and thawing the receiver panel, need to be addressed.

Section 7. Conclusions and Recommendations

Conclusions from the engineering tests provide data for central receiver designers. The testing of the MSEE receiver in an external configuration showed that an external molten salt receiver can be operated under all weather conditions. Basic operation of an external receiver will depend only on thermal losses from the re-

ceiver during cold flow (with no incident flux). Since the molten salt cold tank is nominally 550 ° F, the salt would have to drop nearly 100 ° F before freezing, nearly impossible in any receiver design using 1050 ° F molten salt outlet temperatures. The temperature drop across the MSEE external receiver under no-flux conditions is approximately 30 ° F. Basic operation of an external receiver is not an issue no matter what the design.

On the other hand, optimized operation of a molten salt receiver will be different for a cavity and an external configuration. Conditions may exist which require shut-down of an external receiver in order to maximize net energy production. To optimize the amount of energy collected over a day, the external receiver could not justify staying in cold flow as long as a cavity receiver. Optimizing energy collection means balancing energy collected with energy lost from electrical parasitics and receiver thermal losses. By maintaining cold flow, the receiver is ready to collect any energy which might be available after a long cloud transient; a lengthy restart of the receiver is not necessary.

The thermal performance of the MSEE external receiver was compared to the cavity receiver using efficiency measurements for each receiver. As expected, the point-in-time thermal efficiency of the cavity receiver is slightly higher than the external receiver. Denoting thermal efficiency as absorbed divided by incident power, for the ssame level of incident power, the efficiency of the cavity receiver is about 9% higher than for the external receiver. Most of the difference is due to higher radiative losses from the external receiver.

Convective losses from the MSEE were measured and compared to predictions from correlations. The measured losses are 10% to 100% lower than predictions, most likely due to correction factors in the predictions to account for surface roughness and wind direction. MSEE data indicate that a $\pi/2$ surface roughness factor should not be included in either the natural or forced convection correlations. A factor of between 1.5 and 2 to account for the directional effects of forced convection does seem appropriate. Calculations show a decrease in thermal efficiency between 2% and 8% as wind speed increases from zero to thirty miles per hour. The range of efficiency decrease depends on how the convective coefficients are calculated.

Overnight conditioning, serpentine fill, cold receiver fill, and operation at high flux levels were demonstrated in this experiment. Serpentine fill, cold receiver fill and high flux levels are viable operational strategies which could be implemented for a receiver such as the MSEE external receiver. Overnight conditioning demonstrated the concept of circulating warm salt to keep the receiver warm overnight to prepare for sunrise start-up. However, from an optimized energy collection standpoint, the MSEE receiver is not conducive to such an operating strategy. The thermal energy loss from the overnight exposure of the receiver panel exceeded the energy gained from sunrise start-up.

In summary, the MSEE External Receiver Test Program demonstrated safe, reliable operation of an exposed, molten salt solar central receiver.

Future central receiver development tests can benefit from the experience derived in the MSEE receiver test program. The following is a list of recommendations.

1. More operational data are necessary to verify annual performance estimates.
2. Varying aimpoint strategies provides testing flexibility but requires careful study and implementation.
3. HELIOS or a similiar computer code should be coupled with aimpoint strategy development.
4. Incident flux should be measured and correlated to total power.

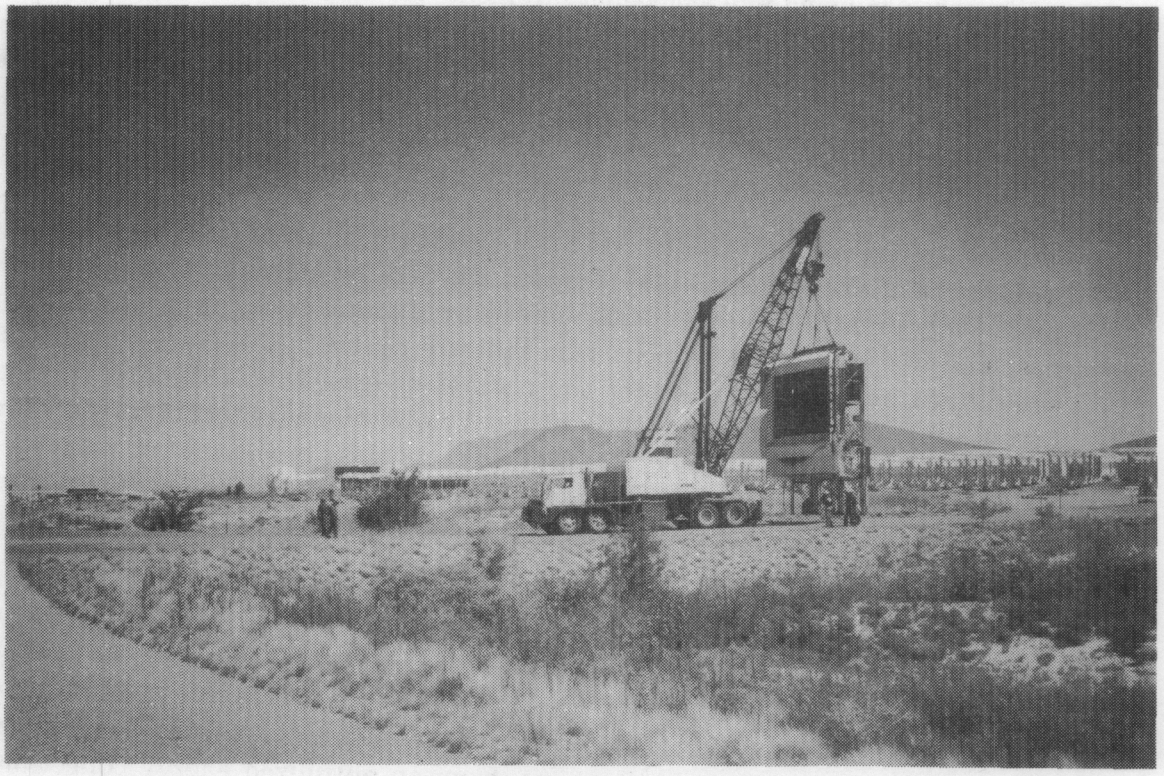

REFERENCES

1. R. Holl, D. Barron, S. Saloff, McDonnell Douglas Corporation, "Molten Salt Electric Experiment (MSEE) Final Report," To be published by Electric Power Reseach Institute.

2. Martin Marietta Corporation, "Molten Salt Electric Experiment Phase I Report, Volume 1,2,& 3," Sandia National Laboratories, SAND 85-8175, September, 1985.

3. C. Maxwell, G. P. Mulholland, "Comparison of Energy Predictions Made by the HELIOS Computer Code to Experimental Data from the Central Receiver Test Facility," Sandia National Laboratories, Internal Memorandum, RS 6220-85-001, November, 1985.

4. D. Dawson, "Revised Physical Property Values for Molten Nitrate Salts," Memo to Distribution, April 26, 1982.

5. R. B. Abernathy, et al., Pratt & Whitney Aircraft, and J. W. Thompson, Jr., ARO, Inc., Measurement Uncertainty Handbook, revised 1980.

6. D. D. Sayers, "Estimation of Convective Losses From Solar Central Receivers," Sandia National Laboratories, Internal Memorandum, RS 8245/17, March, 1985.

7. R. F. Boehm, "Review of Thermal Loss Evaluations of Solar Central Receivers," Sandia National Laboratories, SAND 85-8019, April, 1986.

8. R. Boehm, H. Nakhaie, N. Bergan, "Flux-Off Convective Heat Loss Evaluation of the MSEE External Receiver," ASME Winter Annual Meeting, 1986, to be published.

9. W. Delameter, N. Bergan, "The Molten Salt Electric Experiment: A Project Overview," Sandia National Laboratories, to be published.

10. Falcone, P.K., "A Handbook For Solar Central Receiver Design," Sandia National Laboratories, SAND 86-8006, to be published.

11. Vittitoe, C.N., Biggs, F., " A User's Guide to HELIOS: A Computer Program for Modeling the Optical Behavior of Reflecting Solar Concentrators," Sandia National Laboratories, SAND81-1180, August, 1981.

12. B. Kistler, "Modified Allowable Flux Limits on Receiver Tubes," Memo to Distribution, Sandia National Laboratories, June 4, 1985.

13. Dawson, D.B., "Optimized Solar Central Receiver Design Studies," Sandia National Laboratories, to be published.

14. Cheryl Maxwell, private conversation, 1985-86.

APPENDICES A AND B

TESTING OF THE MOLTEN SALT ELECTRIC EXPERIMENT SOLAR CENTRAL RECEIVER IN ITS EXTERNAL CONFIGURATION

Nina E. Bergan

APPENDIX A – SELECTION OF AIMING STRATEGIES FOR CAVITY TO EXTERNAL COMPARATIVE TEST

The aimpoint used during MSEE testing before the external test program, was a single aimpoint located approximately 1 meter in front of the cavity aperture, using all 211 available heliostats. Although this aiming strategy provided design conditions of approximately 5 MW_{th} to the aperture and 0.6 MW/m^2 peak flux to the absorber panel, the internal spillage (flux incident directly on the uncooled cavity walls) was very high, 14% of the incident power. Some of this energy re-radiates back to the absorber panel, but some is lost. Internal spillage penalizes cavity efficiency because not all power incident through the aperature sees the absorber panel, and cavity efficiency is based on power incident through the aperture. Internal spillage is especially penelizing for the MSEE receiver because of its design - a billboard absorber panel surrounded by an insulated shroud - versus newer designs which make cavity walls actively cooled surfaces. The external receiver efficiency is not affected by spillage because the efficiency is calculated using only the power incident on the absorber surface.

In order to minimize internal spillage, the cavity receiver was operated using an aimpoint which eliminated the back row of CRTF heliostats - those which produce a large beam on the receiver target. As a result of this aimpoint, only 4 MW_{th} of the 5 MW_{th} CRTF heliostat field was used.

The selection of the Cavity Comparative Aimpoint dictated parameters of the External Comparative Aimpoint. In order to reduce uncertainty in the efficiency calculation, the total power of the External Comparative Aimpoint was set equal to the total power to the cavity aperture in the Cavity Comparative Aimpoint. This way, we take advantage of the low *relative* uncertainty of incident power ($\pm 5\%$).

The uncertainty in incident power is the major contributor to the uncertainty in receiver efficiency. For the MSEE receiver, incident power is calculated using HELIOS computer code. The accuracy of the HELIOS incident power calculation is estimated to be $\pm 5\%$ to 20%. These numbers are extrapolated from tests performed during the summer of 1985 at the CRTF comparing HELIOS predictions to data from a flux gage array located on the tower [Maxwell, et al. 1985]. These tests used only aligned heliostats. The 20% estimate is probably overly conservative, but during the MSEE External Test Program, one fourth of the field was still unaligned. We hope that future flux gage array tests will confirm an accuracy of around 10% after all the heliostats are aligned.

In order to distinguish actual differences between cavity and external performance, the uncertainty in the receiver efficiency must be minimized. Receiver thermal efficiency is defined to be absorbed divided by incident power.

$$\eta = \frac{Q_{abs}}{Q_{inc}} \qquad (A-1)$$

There are two ways to compare the receiver efficiency: using the absolute values of efficiency, or using relative values of efficiency. The high relative accuracy of HELIOS makes the second method much more accurate than the first. The following example will clarify this point.

Method I: Absolute value of efficiency. The difference between the absolute value of the cavity and external efficiencies is:

$$\left(\eta_{cav} - \eta_{ext}\right)_I = \frac{Q_{abs,cav}}{Q_{inc,cav}} - \frac{Q_{abs,ext}}{Q_{inc,ext}} \qquad (A-2)$$

Using a root sum square technique to evaluate the uncertainty, $\delta\left(\eta_{cav} - \eta_{ext}\right)_I$,

$$\delta\left(\Delta\eta_I\right) = \sqrt{\left(\frac{\delta Q_{abs,cav}}{Q_{inc,cav}}\right)^2 + \left(\frac{-\delta Q_{abs,ext}}{Q_{inc,ext}}\right)^2 + \left(\frac{-Q_{abs,cav}}{Q^2_{inc,cav}}\delta Q_{inc}\right)^2 + \left(\frac{Q_{abs,ext}}{Q^2_{inc,ext}}\delta Q_{inc,ext})^2\right)^2} \qquad (A-3)$$

$$\delta\eta = \sqrt{\left(\frac{1}{Q_{inc}} \cdot \delta A_{abs}\right)^2 + \left(\frac{Q_{abs}}{(Q_{inc})^2} \cdot \delta Q_{inc}\right)^2} \qquad (A-4)$$

Using the following values for uncertainties in the absolute value of incident and absorbed power:

$$\delta Q_{inc} = \pm 15\%$$

$$\delta Q_{abs} = \pm 5\%$$

$$\left(\delta m = \pm 5\%,\ \delta(\Delta T) = \pm 1\%,\ \delta C_p = \pm 1\%\right)$$

Results in

$$\delta\left(\eta_{cav} - \eta_{ext}\right)_I = \pm 18\%$$

Method II: Relative value of efficiency, assuming incident power of cavity equals incident power of external:

$$\left(\eta_{cav} - \eta_{ext}\right)_{II} = \left(\frac{Q_{abs,cav} - Q_{abs,ext}}{Q_{inc}}\right) = \left(\frac{\Delta Q_{abs}}{Q_{inc}}\right) \qquad (A-5)$$

Again using the Root-Sum-Square Method to evaluate uncertainties, the uncertainty in the difference, $\delta\left(\eta_{cav} - \eta_{ext}\right)_{II}$ is:

$$\delta\left(\eta_{cav} - \eta_{ext}\right)_{II} = \sqrt{\left(\frac{\delta Q_{abs,cav}}{Q_{inc}}\right)^2 + \left(\frac{\delta Q_{abs,ext}}{Q_{inc}}\right)^2 + \left(\frac{Q_{abs,cav} - Q_{abs,ext}}{Q_{inc}^2}\delta Q_{inc}\right)^2} \qquad (A-6)$$

Using the following values for uncertainty (δ) in the *relative* values (Δ)of absorbed and incident powers:

$$\delta\Delta Q_{inc} = \pm 5\%$$

$$\delta\Delta Q_{abs} = \pm 5\%$$

Results in

$$\delta\left(\eta_{cav} - \eta_{ext}\right)_{II} = \pm 6\%$$

This example shows the advantage of making the cavity to external comparison on a relative rather than absolute basis. The expression for the uncertainty of the difference (Method II) contains one less term than the expression for the uncertainty of the absolute value (Method I). Also, the uncertainty in the *difference* of incident power, ($\delta\Delta Q_{inc} = \pm 5\%$), is much lower than the uncertainty in the *absolute* value of incident power, ($\delta Q_{inc} = \pm 15\%$).

To summarize, in this experiment cavity and external receiver efficiencies are compared using Method II outlined above. This method takes advantage of the low *relative* uncertainty in incident power.

APPENDIX B - EFFICIENCY CALCULATIONS

Receiver thermal efficiency is defined to be absorbed divided by incident power.

$$\eta = \frac{Q_{abs}}{Q_{inc}} \qquad (B-1)$$

The incident power on the receiver, Q_{inc} changes with insolation, day of year, time of day, heliostat reflectivity and the number of heliostats aimed at the receiver. The following section shows how data from five HELIOS runs, ±4 hrs, ±2hrs, and solar noon, for a given aimpoint, is curve fit, then corrected for heliostat reflectivity, and insolation. In all cases, the test data was from such a short period of time, that incident power was assumed to not vary with day of year.

Cavity Comparative Aimpoint data was taken from day 140 to day 143. HELIOS predictions are for day 143 and there is no need to make further correction for day of year. We curve fit HELIOS data to find an expression for total power to cavity aperture, Q_{inc} (MW), as a function of solar time, t (hrs) where 0 is solar noon:

$$Q_{inc}(t) = 3.98 + .5051E-7 \cdot t - .0475 \cdot t^2 - .4462E-8 \cdot t^3 - .0018 \cdot t^4 \qquad (B-2)$$

The HELIOS predicition obtained from the above equation was multiplied by 0.97 to account for the difference in target size between the cavity aperture and the external absorber panel. Since HELIOS assumes perfect mirrors and perfect alignment, spillage will always be underpredicted. The 0.97 factor equilibrates the underprediction for the cavity and absorber panel.

External Comparative Aimpoint data was taken from day 178 to day 192. HELIOS predictions are for day 177 and there is no need to make further corrections for day of year. We curve fit HELIOS data to find an expression for the total power to the absorber panel, $Q_{inc}(t)_{HEL}$, (MW), as a function of solar time, t(hrs) where 0 is solar noon:

$$Q_{inc}(t) = 3.98 - .3153E-8 \cdot t - .037 \cdot t^2 - .1687E-9 \cdot t^3 - .0013 \cdot t^4 \qquad (B-3)$$

External Optimized Aimpoint data was taken from day 193 to day 206. HELIOS predictions are for day 200 and there is no need to make further correction for day of year. Curve fit HELIOS data to find expression for total power to absorber panel, $Q_{inc}(t)$ (MW), as a function of solar time, t(hrs) where 0 is solar noon:

$$Q_{inc}(t) = 4.97 + .504E-7 \cdot t - .040 \cdot t^2 - .4509E-8 \cdot t^3 - .0023 \cdot t^4 \qquad (B-4)$$

The average heliostat reflectivity, ρ, (was 80.5%) in April/May, and 80.14% in July. HELIOS assumes reflectivity is 80.0% . A correction factor $\left(\frac{\rho}{0.80}\right)$ was used for each aimpoint.

HELIOS predicitions assumed insolation, I, to be 950 W/m^2. A correction factor $\left(\frac{I}{950}\right)$ was used to account for measured insolation.

The actual number of heliostats on target during any test is always less than the full field, due to maintainence and repairs. Sensitivity studies were performed to determine the best way to correct HELIOS predictions for the actual number of heliostats on target. The calculation is so insensitive to individual heliostats that it is sufficient to multiply HELIOS total power prediciton by a ratio of the actual number of heliostats on target, #HOT, versus the total field for that particular aimpoint. Note the External Comparative Aimpoint uses 173 heliostats, the Cavity Comparative Aimpoint uses 182 heliostats, and the Optimized External Aimpoint uses all 211 heliostats.

The equation to determine actual power, $Q_{inc,act}$ to the receiver for the Optimized External Aimpoint can be written as:

$$Q_{inc,act} = Q_{inc}(t) \cdot \left(\frac{\rho}{0.80}\right)\left(\frac{\#HOT}{211}\right)\left(\frac{I}{950.}\right) \qquad (B-5)$$

To calculate receiver efficiency, we need the power absorbed by the salt, which is simply the change in enthalpy of the salt:

$$Q_{abs} = mC_p(T_{out} - T_{in}) \qquad (B-6)$$

where m is the mass flow rate of the salt, corrected from raw data to match sump depletion calibrations made during the test program:

$$m_{\text{true}}(\text{klb/hr}) = 6.4 + .9388 m_{\text{meas}}(\text{klb/hr}) \qquad (B-7)$$

The specific heat is calculated from [Dawson, 1982]:

$$C_p(\text{BTU/lb}_\text{m}\text{F}) = .3449 + .22857\text{x}10^{-4} \cdot T(F) \qquad (B-8)$$

The receiver efficiency, η is then the absorbed power divided by the actual power incident on the receiver, calculated above as $Q_{\text{inc,act}}$.

APPENDIX C—HELIOSTAT AIMING STRATEGIES AND THERMAL-HYDRAULIC RECEIVER ANALYSIS

By: Tibor Buna
Solar Power Engineering Company
Contract SNLA 65-8876

edited by: Nina E. Bergan

Abstract

Four heliostat aiming strategies were developed for the MSEE External Receiver Test Program. The algorithm used maps the heliostat field onto the target. A thermal-hydraulic analysis was performed to verify the receiver tube and salt temperatures with these aiming strategies. Results from this analysis were also used to calculate representative front surface receiver temperatures. These temperatures are important for radiative and convective heat loss calculations.

Section 1. Summary

The purpose of this appendix is to document the analyses and data generated by Solar Power Engineering Co. (SPECO) in support of the MSEE Phase III External Receiver Test Program. It covers two activities: the development of heliostat aiming and thermal-hydraulic analysis on the receiver.

The aiming strategies are discussed in Section 2. The approach and methodology are described, and aiming strategies for three basic test configurations - "comparative cavity," "comparative external," and "optimized external" - are developed. The two other tests - "high-flux" and "flux-on convective loss" - also discussed in this report, used slightly modified versions of these basic strategies. Due to constraints imposed by the non-optimized receiver design, the comparative test requirements could only be met at partial loads, i.e., by turning off some of the heliostats. It is shown, however, that relatively minor changes (not within scope of the program) in the location and dimensions of the aperture could have eliminated this problem. A more general implication of this result is that, in a north-field solar central receiver, an optimized cavity enclosure exists. (This statement is consistent with the results of the comparitive tests.)

The thermal-hydraulic analysis discussed in Section 3 verified the aiming strategies by showing that the tube metal temperatures in the receiver are within design limits. The temperatures and temperature gradients during the high-flux test were found to be acceptable for short exposures, but marginal for long-term service. A special study was conducted to determine the effect of skewed flux distributions on temperatures and efficiency. It was found that - contrary to intuitive expectations - skewing the peak fluxes towards the hot end of the salt loop reduces losses and increases efficiency.

Thermal-hydraulic analysis was performed in support of convective loss tests (Section 4). The objective was to provide temperature and radiation loss data as a part of the data reduction and analysis effort.

Section 2. Aiming Strategy Development

Definition– An aiming strategy may be defined as the specification of heliostat aim point coordinates on a reference surface, as a function of heliostat locations. The objective is to achieve a desired flux distribution on the receiver surfaces.

In the current study the reference surface was selected to be a vertical plane going the center of the aperture of the cavity configuration. This plane coincides closely to the receiver aperture plane which has a slight tilt with respect to the vertical.

Objectives– A summary of test conditions and specific objectives of the associated aiming strategies are listed in Table C-1. The thrust of this analytical effort was the development of the aiming strategies for the comparative and the external optimized receiver tests. The strategies for the high-flux and convective tests are slight

modifications of the former, as indicated in Table C-1.

TABLE C-1
AIM POINT STRATEGIES - SUMMARY

Test Description	Aim Point Strategy Objectives	Remarks
Comparative Peformance Tests – Cavity vs. External Configuration	Cavity - Minimum internal spillage (From 15% to less than 5%) - Comply with peak flux design criteria - Comply with salt and metal temperature limits	Due to constraints imposed by existing cavity geometry, some heliostats were turned off to meet requirements.
	External - Equalize power: Incident flux on external panel = flux through cavity aperture - Equalize peak fluxes on external and cavity panels - Comply with salt and metal temperature criteria	Constraints were set by comparative cavity aiming strategy. Some heliostats turned off.
Optimized (Full-Power) External Receiver Performance Tests	- Maximize power (intercept power from full heliostat field) - Minimize spillage - Comply with peak flux and slat and metal temperature limits	Optimize flux distribution. Receiver geometry fixed by existing panel
High-Flux Test	- Provide local peak flux of 1 MW/m^2	Achieved by moving in aimpoints.
Barron's Convection Tests	- Two identical groups of heliostats with 75 heliostats per group	Modified comparative external aiming strategy.

Approach– The principal analytical tool used during these analyses was the minicomputer program DOMAIN developed by SPECO personnel. This CAD-type program employs a double-projection mapping technique to reduce the ray tracing analysis to a geometrical problem. On these maps the flux densities at selected points on the receiver are represented by areas whose boundaries are functions of aim point coordinates. The desire aiming strategies are established by manipulations of these boundaries.

A second program used extensively was HELIOS. A number of HELIOS runs were performed to verify the flux density distributions and spillage losses predicted by DOMAIN. In addition, HELIOS provided the necessary heliostat field reflectivity

parameters to be used in the DOMAIN runs.

Further verification of the aiming strategies was accomplished by the THERMOFLUID program. This analysis was performed to insure that tube metal temperatures were not exceeded. The THERMOFLUID runs are discussed in more detail in Section 3.

Description of Program DOMAIN- The key elements of the program are illustrated in Figure C-1. The "true" shape of the heliostat field is shown in 1a. Upon performing the double projection mapping, the field boundaries appear as depicted by the heavy lines in 1b. The area of the projected field is proportional to the peak flux density (or concentration ratio) achievable at the focal point (e.g., center of aperture) of the heliostats with single-point aiming. The semi-circle represents the theoretical maximium flux density achievable with a semi-infinite heliostat field with perfect focusing, and in the absence of atmospheric attenuation. In comparison, the area of the complete circle would represent the maximum slux achievable with an infinite field focused at the center of a down-facing aperture.

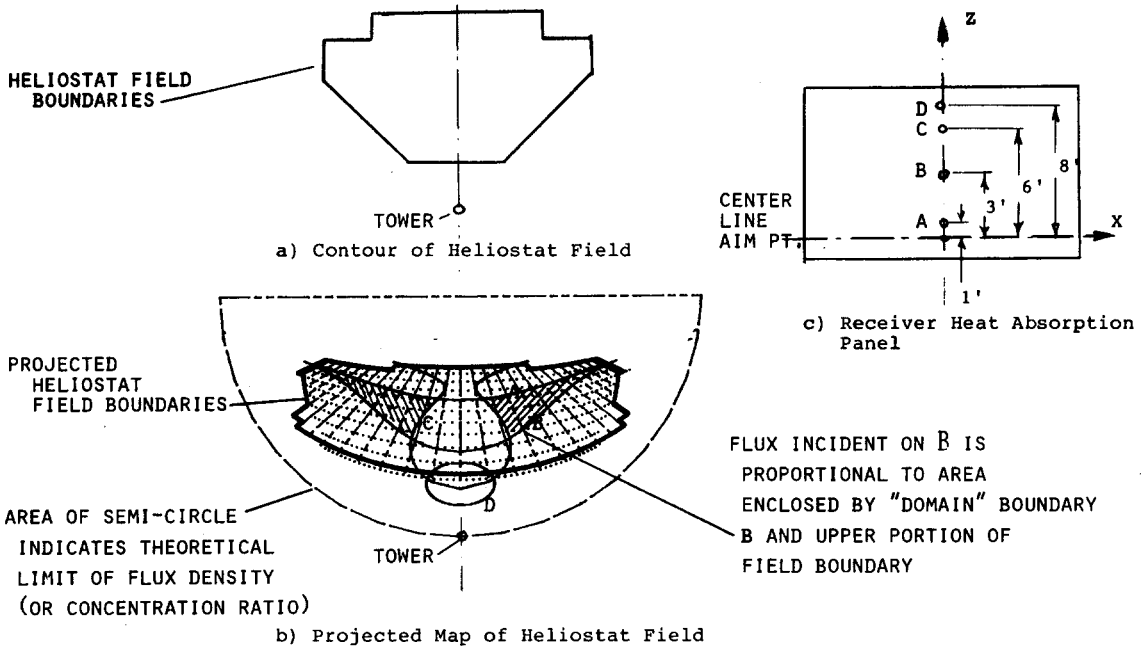

Figure C-1. Elements of Program DOMAIN - The program is based on a double-projection mapping technique which reduces the radiation analysis to a geometrical problem

The curves A, B, C, and D on 1b represent domain boundaries (with single-point central aiming) which together with the field boundaries they intercept, enclose areas proportional to the fluxes incident on points A, B, C, and D on the receiver panel at the locations shown in 1c. The domain boundaries associated with a given point on the receiver enclose those heliostats of the collector field which contribute to the incident flux at that point. It is evident from 1b and 1c that by moving upwards along the panel centerline the flux density first increases, reaching a maximum at B, and then decreases at the higher elevations. It is further evident that the

domain boundaries gradually change their character during this process, going from singly-connected to doubly-connected curves. As indicated by curves C and D, the transition point between these two shapes corresponds to an elevation on the receiver between C and D. It may be shown that this transition point corresponds to the steepest flux gradient along the vertical line connecting A and D.

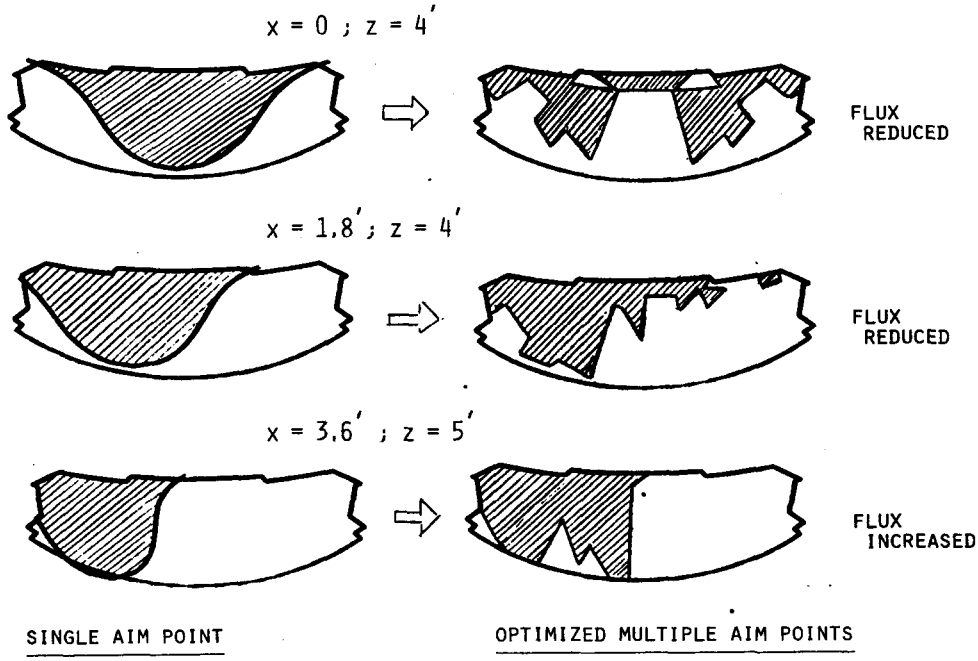

Figure C-2. Flux-Architecture – Flux densities at the (X,Z) points on the receiver and their changes with aiming are indicated by the shaded areas enclosed by DOMAIN boundaries

Since the domain boundaries associated with a given point on the receiver panel are determined by the relative position of the point with respect to the aim point, changing the aim point elevation will cause the domain boundaries (an flux densities) to shift. For example, if the aim points of the heliostats in the shaded area bounded by curves A, B, and C are moved downwards by 2 ft, the flux intensity at point A on Figure C-1 will be increased by an amount proportional to those areas, whereas the intensity at B will be decreased, and that at C will remain unchanged.

This simple example illustrates the basic elements of more complex flux architectures such as shown in Figure C-2. For the three points on the receiver indicated by their respective X, Z coordinates, the desired changes in flux levels were accomplished by changes produced in the respective domain boundaries via (mostly lateral) shifts in aim points.

internal and external spillage for the MSEE cavity configuration*

Another example of a somewhat different use of the program is shown in Figure C-3. The point X=10, Z=5 on the plane of the receiver panel is outside of the heat absorption area, hence fluxes incident on this point represent spillage. The area enclosed by the heavy boundary line in 3a indicates considerable spillage with the old MSEE aim point. By projecting the contour of the aperture on the same

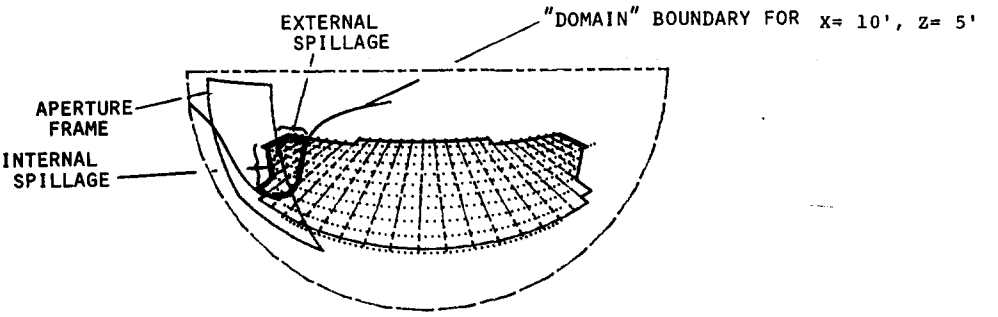

a) SINGLE AIM POINT - 1 M IN FRONT OF APERTURE

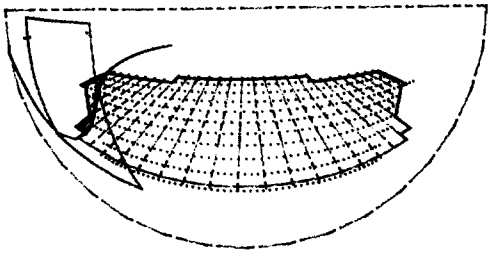

b) SINGLE AIM POINT IN CENTER OF APERTURE

Figure C-3. Sample problem – Evaluation of the effect of aim point location on

map, it becomes evident that approximately half of that spillage is external, and the other half is internal. 3b shows that by moving the aim point into the aperture plane, the total spillage is considerably reduced and its external component is all but eliminated.

Results for the Comparative Tests– The comparative aiming strategy for the cavity configuration is shown in Figure C-4. In order to meet the requirements outlined in Table C-1, eighty heliostats had to be turned off to prevent excessive external spillage and overheating of the aperture frame. This is necessary to minimize internal spillage with the given geometry of this receiver.

The comparative aiming strategy for the external receiver is shown in Figure C-5. In order to match peak flux and total power conditions with the cavity configuration, again a number of heliostats had to be turned off.

Results for the Optimized External Receiver Tests– Figure C-6 shows the aiming strategy for the optimized external receiver. Optimization in the present context means flattening out the incident flux profiles with a plateau near the allowable peak flux level, while maintaining spillage at a minimum. This resulted in maximizing the total incident and absorbed power of the (existing) panel.

Optimization in the broader sense and as applied to new receiver designs, involves the combination of heliostat field boundaries and layout, tower height, receiver geometry, and aiming strategy.

Optimization of the Cavity Receiver– A special study was conducted to determine the modifications required for the MSEE cavity absorption panel to intercept the same amount of direct radiation - with the same aiming strategy - as the optimized external panel. The study was completed with the DOMAIN program using the approach depicted on Figure C-3. Results show that this goal could have been ac-

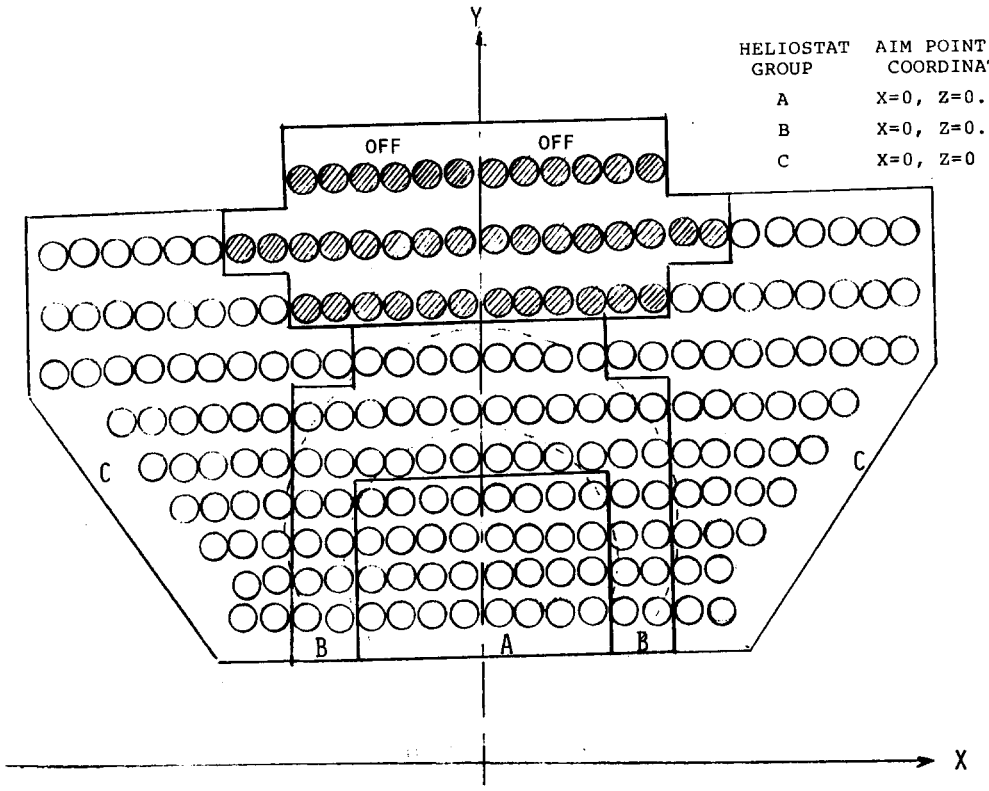

Figure C-4. Comparative aiming strategy - cavity receiver

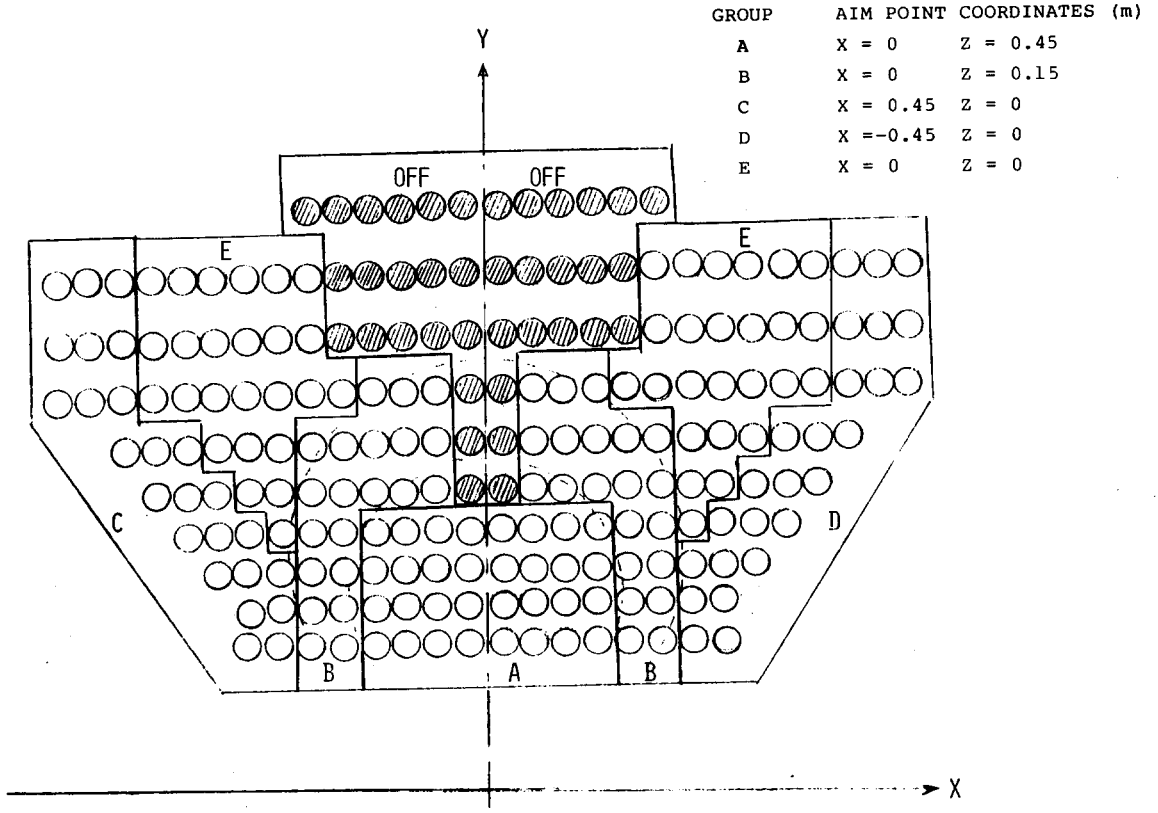

Figure C-5. Comparative aiming strategy - external receiver

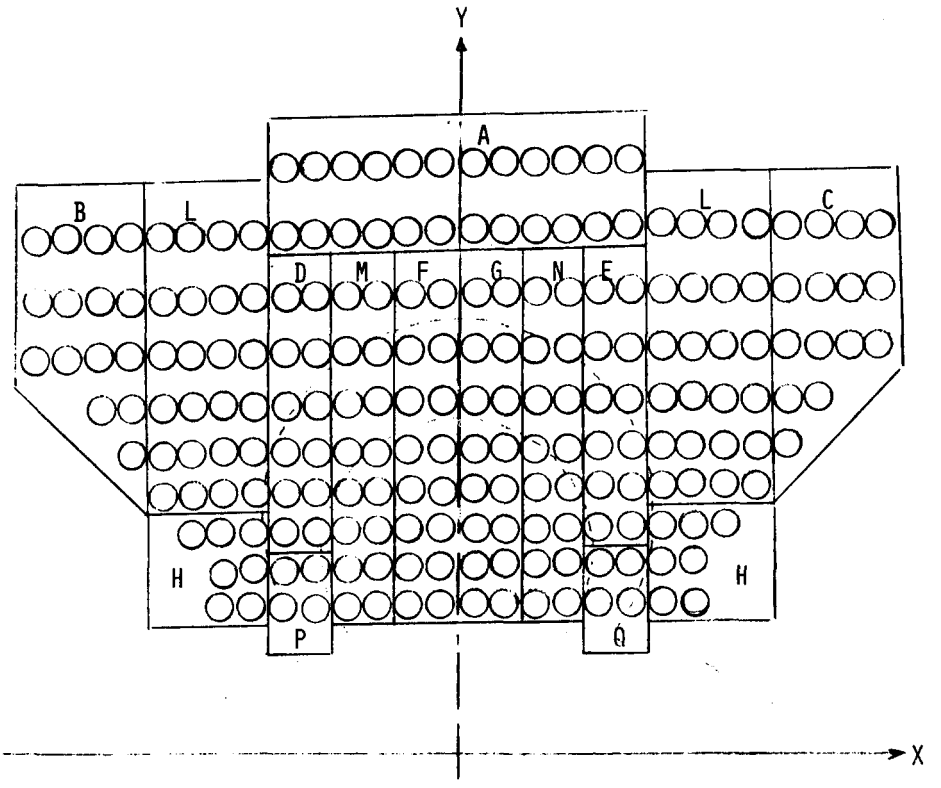

GROUP	AIM POINT COORD. (m) X	Z
A	0	0.61
B	-0.61	0
C	0.61	0
D	-0.3	0
E	0.3	0
F	1.2	0
G	-1.2	0
H	0	-0.61
L	0	0
M	1.1	0
N	-1.1	0
P	-0.3	-6.1
Q	0.1	-6.1

Figure C-6. Optimized (full power) aiming strategy - external receiver

complished with a minor modification consisting of raising the center of the aperture 1.5 ft, and increasing the aperture width by 1 ft. This would increase the aperture area from 9x9 ft to 9x10 ft.

Section 3. Thermal–Hydraulic Analysis

General– Thermal-hydraulic analyses were conducted to support the comparative, optimized, high-flux, and convective tests using the THERMOFLUID program.

THERMOFLUID is a minicomputer program developed by SPECO personnel, which calculates heat transfer and fluid flow parameters and salt- and metal temperature distributions within the heat absorption panel. The principal inputs to the program were the measured salt flow rates, the incident flux density distributions calculated by HELIOS, the thermophysical properties of the salt, and the measured salt inlet and outlet temperatures.

Verification of Aiming Strategies– The salt and tube temperature profiles for the comparative and optimized external tests as determined by THERMOFLUID are shown in Figures C-7, C-8, and C-9. The main interest here is to show that, with the flux density distributions provided by the respective aiming strategies, the ID and OD temperature limits are not exceeded. The limits shown on the figures have been conservatively established for long life service during previous studies.

The program also calculates the linear- and fourth-power averages of the tube front surface temperatures. The linear average is indicative of convection losses, whereas the forth-power average reqpresent an equivalent flat plate temperature that would result in an emitted infrared (IR) radiation loss equal to that from

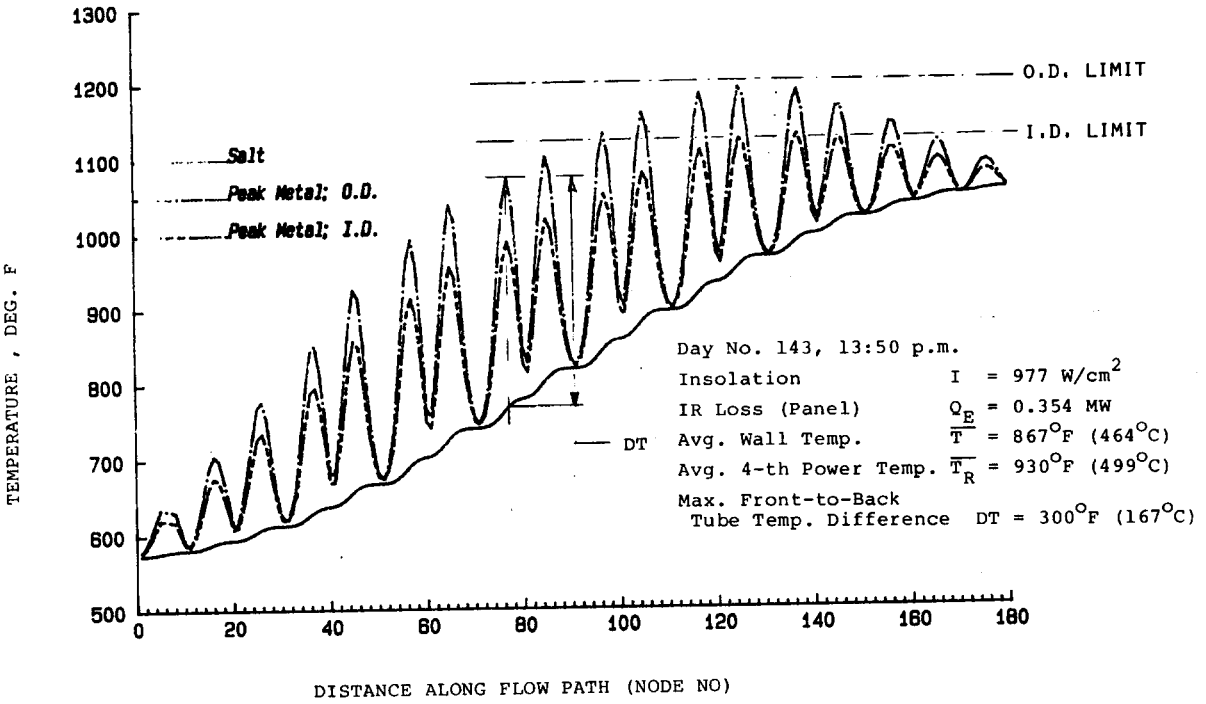

Figure C-7. Temperature profiles – cavity receiver, comparative test

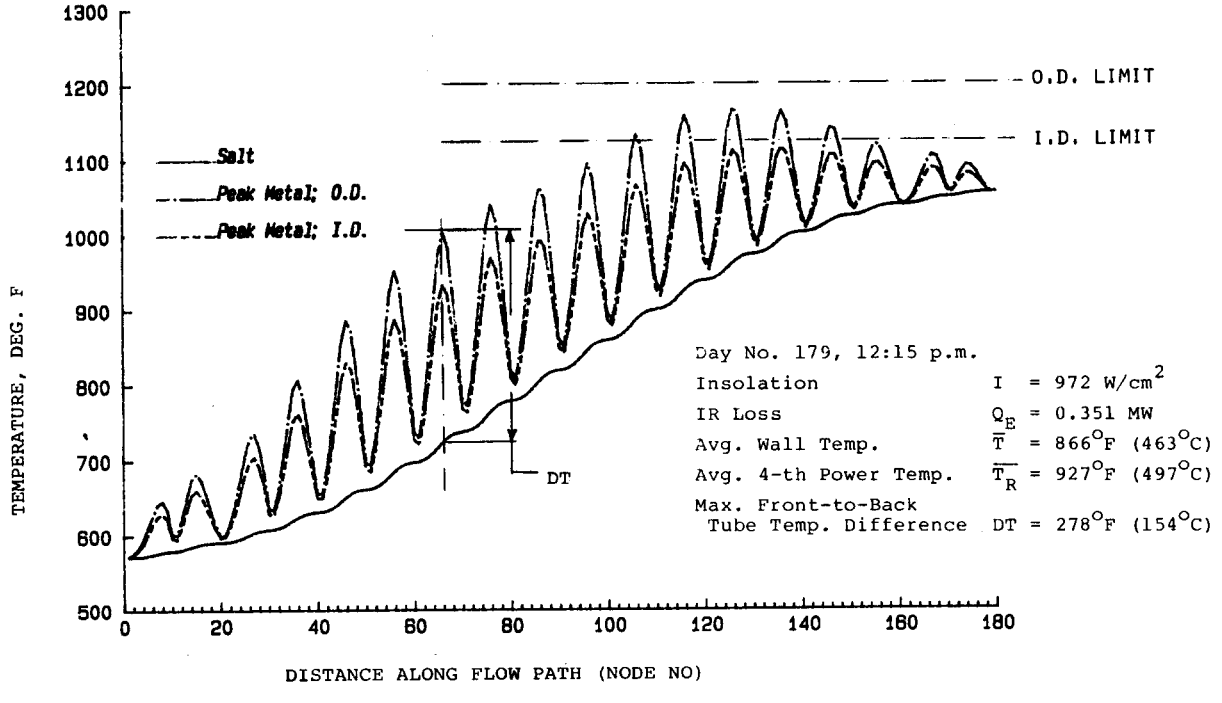

Figure C-8. Temperature profiles – external receiver, comparative test

the tubular panel. The calculation of this temperature takes into account both the longitudinal and circumferential tube temperature gradients, as well as local shading and blocking by adjacent tubes. Note that in the case of the cavity receiver, the IR loss, Q_E, represents emission from the panel itself, and not the net loss through the aperture.

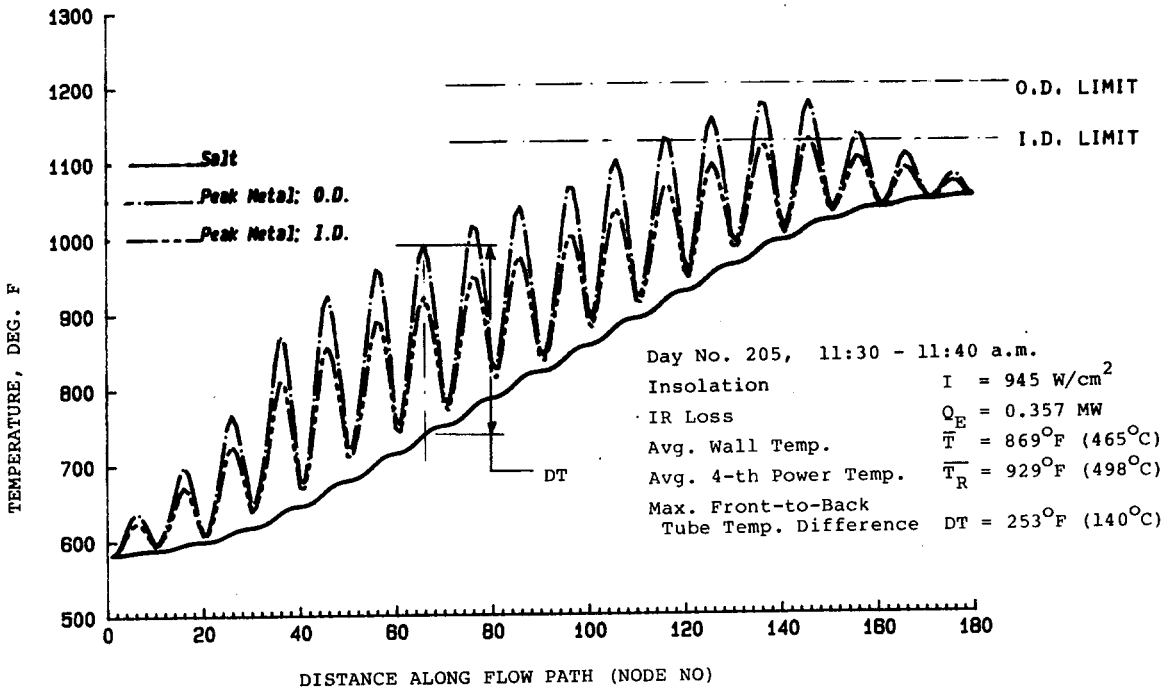

Figure C-9. Temperature profiles – optimized external receiver

The front-to-back tube wall temperature difference is the main source of thermal stresses in the tubes, and is an important parameter in thermo-structural analyses. An evaluation of the effect of this parameter on the life of the receiver was outside the scope of this study; however, the range of values calculated for these tests are consistent with the previous operational history of this receiver.

For the optimized external aimpoint, note the temperature difference between the salt and the tube crown. The difference, labeled DT in the figure, is both smaller than with the other aimpoints and almost constant across the middle two-thirds of the pond. This is indicative of the flat flux density distribution achieved by the aiming strategy shown in Figure C-6.

High-Flux Test– The temperature profiles for the high-flux test are shown in Figure C-10. The ID and OD limits have been exceeded by 3° F and 30° F (0.3% and 3.%) respectively, and the maximum front-to-back tube temperature difference is nearly 400° F, compared to 250° to 300° F in previous tests. These predicted temperatures are not high enough to cause concern during the short test conducted here. However, further analysis would be required before using this aimpoint on a long-term basis.

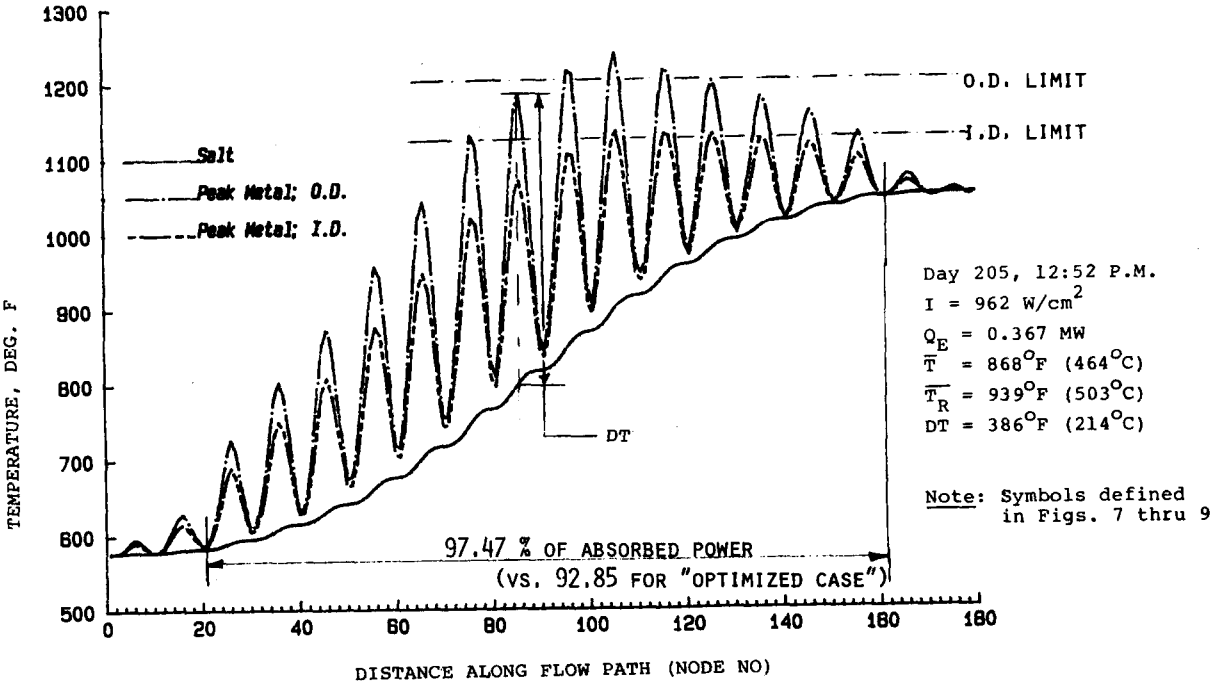

Figure C-10. Temperture profiles – high flux test

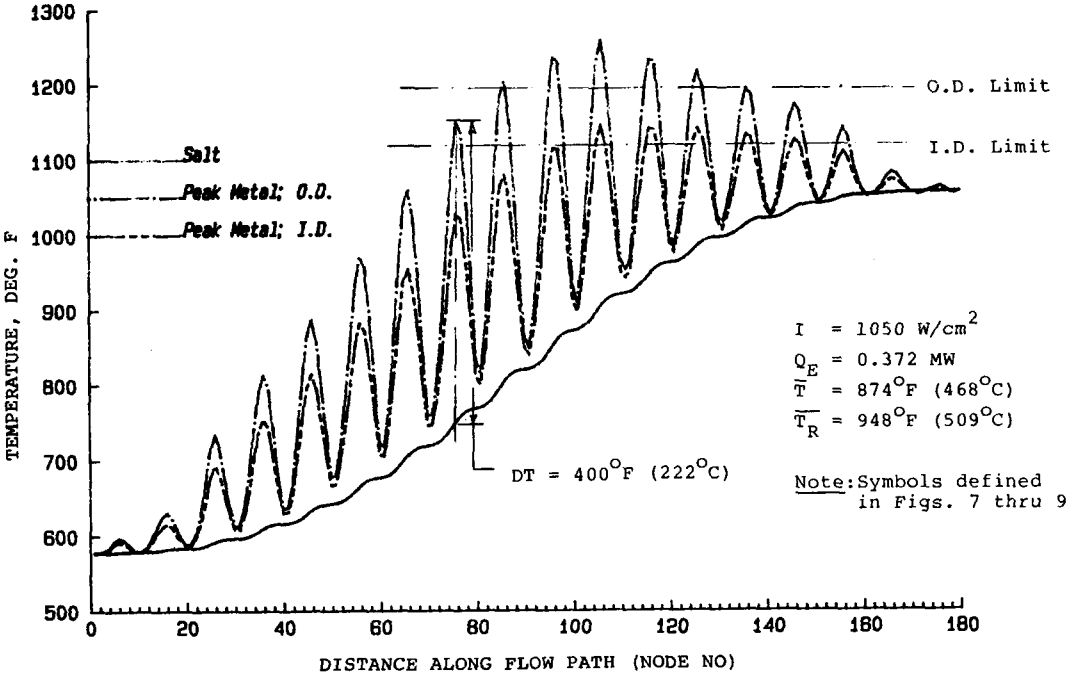

Figure C-11. Temperature profiles – high flux test, adjusted to 1050 W/cm^2 insolation

Figure C-11 shows the effect of further increasing the flux intensities by raising the insolation level from 962 W/cm^2 prevailing during the actual test to the peak design value of 1050 W/cm^2, with the same aiming strategy. The maximum front-to-back temperature difference increases 4%, and the O.D. temperature limit is exceeded by 60° F, twice as much as before.

Effect of Flux Distribution Skewing on Efficiency- A question was raised during this program as to the optimum shape of the flux density distribution on a receiver panel. The flux distribution can be a trapezoidal profile with peak fluxes biased towards the center, or the hot, or the cold side of the receiver. The analysis performed here shows, from a standpoint of thermal efficiency, the optimum profile is skewed towards the hot end of the salt temperature profile.

The flux distribution used for this analysis was derived from Barron's convection test aimpoint. In this aimpoint only aligned heliostats were used, which resulted in an asymmetric pattern of operational heliostats, and a flux distribution skewing on the receiver panel towards the hot end. This is shown as Case a on the top diagram in Figure C-12. Case b on the same diagram is the mirror image of the former, and represents a distribution skewed toward the cold end, at the same total incident power level. The number of heliostats in Barron's convective aimpoint was increased to more clearly show the difference in peformance between the Case a and Case b. The incident power levels were chosen to yield 2.82 MW absorbed power and peak ID temperatures just reaching the allowable limit. Results for both cases are shown by the THERMOFLUID plots in Figure C-12.

Note that, for the same output, the emission loss in Case b is 11% higher than in Case a, and the average tube temperature (indicative of convection losses) is 48 degrees higher in Case b than in Case a. These results indicate that the thermal efficiency of a receiver is increased by skewing the peak fluxes towards the hot end of the salt loop.

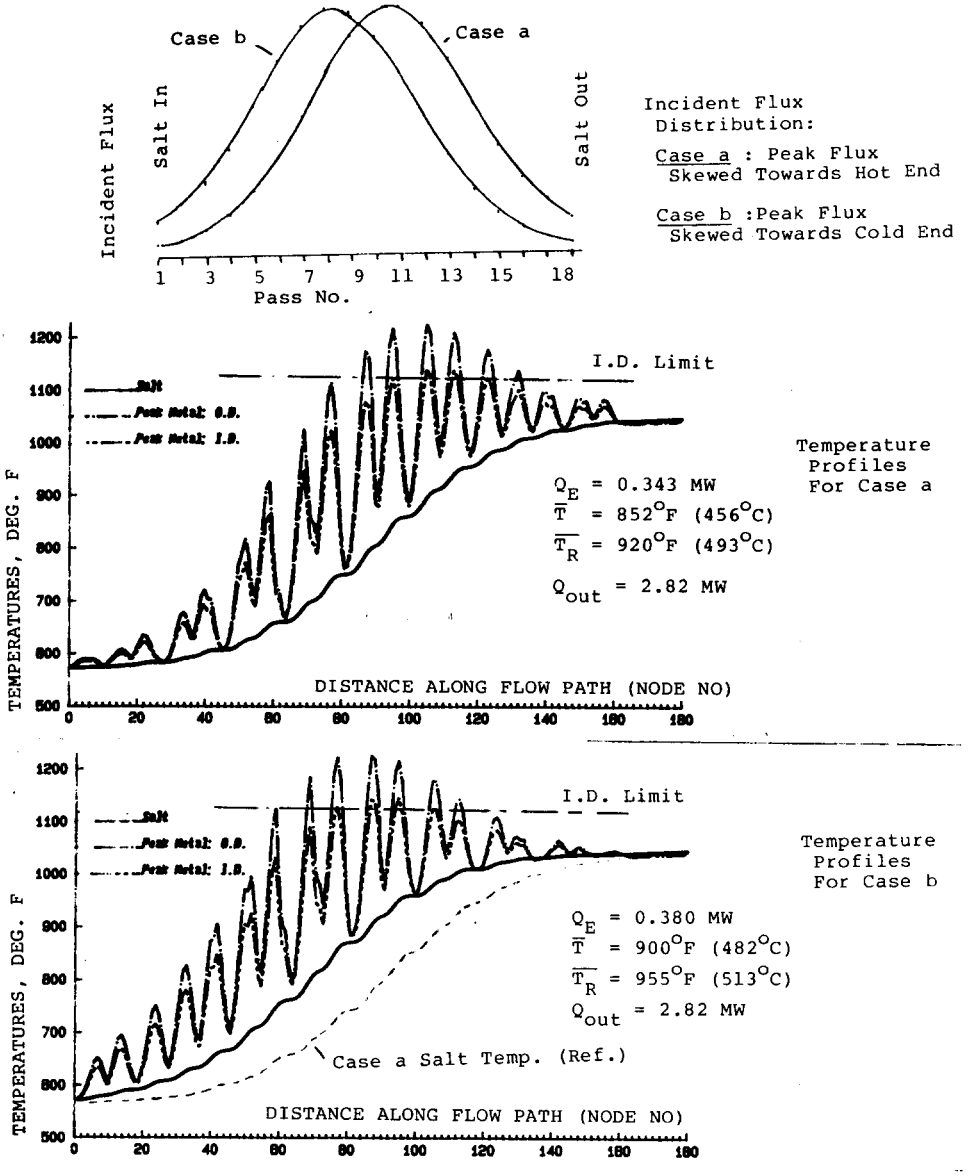

Figure C-12. Effect of skewing of flux distribution on receiver thermal efficiency

APPENDIX C REFERENCES

1. K. J. Beninga and T. Buna, "In Situ Evaluation of Convective Losses in Molten Salt Central Receivers," Proceedings of the 1984 Annual Meeting, American Solar Energy Society, Inc., 1984, p. 215.
2. Phase 3 Summary Report, Solar Test at CNRS Test Facility, France, MCR-76-133 (Issue 3), June 1977.
3. "Alternate Central Receiver System, Phase II," Final Report, Sandia Contract 18-6879C, May 1981.

APPENDIX D–CAVITY WALL TEMPERATURES: MEASUREMENT AND CALCULATION

By: Prof. L. K. Matthews and R. Sierra
Department of Mechanical Engineering
New Mexico State University
Contract SNLA 32-7347

edited by: N. E. Bergan

Abstract

The placement and use of thermocouples in semitransparent fibrous materials (such as alumina-silica) used in solar central receivers has been studied and results are presented. The effects of thermocouple shielding and placement are considered. Measurements are compared to computer generated predictions of the temperature profile in the materials. Experimental data matches predicitons within ±10% when radiation shields are applied to the thermocouples.

Section 1. Summary

Fibrous insulating materials, such as alumina-silica and zirconia, have been studied on several occasions[1,2,3,4]. In some of these studies[2,3,4], attempts have been made to measure the temperature in the semitransparent materials subjected to concentrated sunlight.

The present study was motivated by the need to estimate surface temperatures in the cavity of the Molten Salt Electric Experiment (MSEE) solar central receiver tested at the Central Receiver Test Facility in Albuquerque, New Mexico[5]. In this experiment several type K (chromel-alumel) thermocouples were installed in the alumina-silica insulating materials lining the receiver cavity. The thermocouples were installed from the back of the receiver walls. Alumina cement provided a radiation shield for transmitted and scattered solar radiation.

To understand the effect of radiation shields on thermocouple measurements, experiments were conducted at the New Mexico State University Solar Furnace[6]. In these experiments we also studied the effect of installing the thermocouples from the back, along a temperature gradient, rather than the side, in an isothermal plane. We compared the data from these tests to predictions from the computer code TOTAL[7]. This code was then used to estimate the temperature distribution in the MSEE receiver.

Section 2. Fibrous Insulating Material

The insulating material used in the MSEE solar receiver is Babcox and Wilcox blanket type B1800. It has a density of 96.11 kg/m^3 (6 lb/ft^3) and a use limit of 1255 K (1800° F). As has been shown[1], this material is semitransparent to visible radiation. This means that any temperature measuring device must be shielded from the radiation, or severe measurement errors can occur. In addition, the peak temperature actually occurs inside the material, not on the front surface.

A radiation shield requires a material which has a thermal conductivity and specific heat similar to the material being tested. In addition, the shield must be opaque to the solar radiation and have radiative properties similar to the material being tested. Thermocouple sheaths will have radiative properties closer to the thermocouple metal than the alumina-silica. For this study, an alumina cement was chosen for the shield since it is dense enough to be opaque to the radiation while having a conductivity and reflectance similar to the alumina-silica material being tested. The thermocouple was kept small (30 gage wire), thereby keeping the shield small. This was necessary because although the shield is obviously better

than having no shield it will still disrupt the scattered radiation field in the material. Scattering is significant in these materials and any measures that can be taken to reduce the effects of the thermocouple being in the material are warranted. To be sure that the thermocouple did not move in the material and that no undesireable air gap existed around the thermocouple, the outer layer of the shield was slightly moist when it was installed. This allowed the thermocouple to become part of the material.

Section 3. Solar Testing of the Materials

Testing of the 2.54 cm (1 inch) thick alumina-silica materials was performed at the NMSU Soloar Furnace (NMSU SF)[6]. These materials were supplied by Sandia National Laboratories. The objectives of the tests were to:

1. Compare shielded vs. nonshielded thermocouples,
2. Compare side vs. back mounted thermocouples,
3. Determine thermocouple placement effects,
4. Acquire data in the middle and front planes of the material,
5. Compare measurements with calculations,
6. Gain confidence in the accuracy of MSEE temperature calculations.

Thermocouples were placed in the middle plane of the material (1.25 cm from the front surface) for some of the measurements and in the front plane of the material (0.64 cm from the front surface) for other measurements. The solar flux was incident on the front of the material and the back side was exposed to ambient.

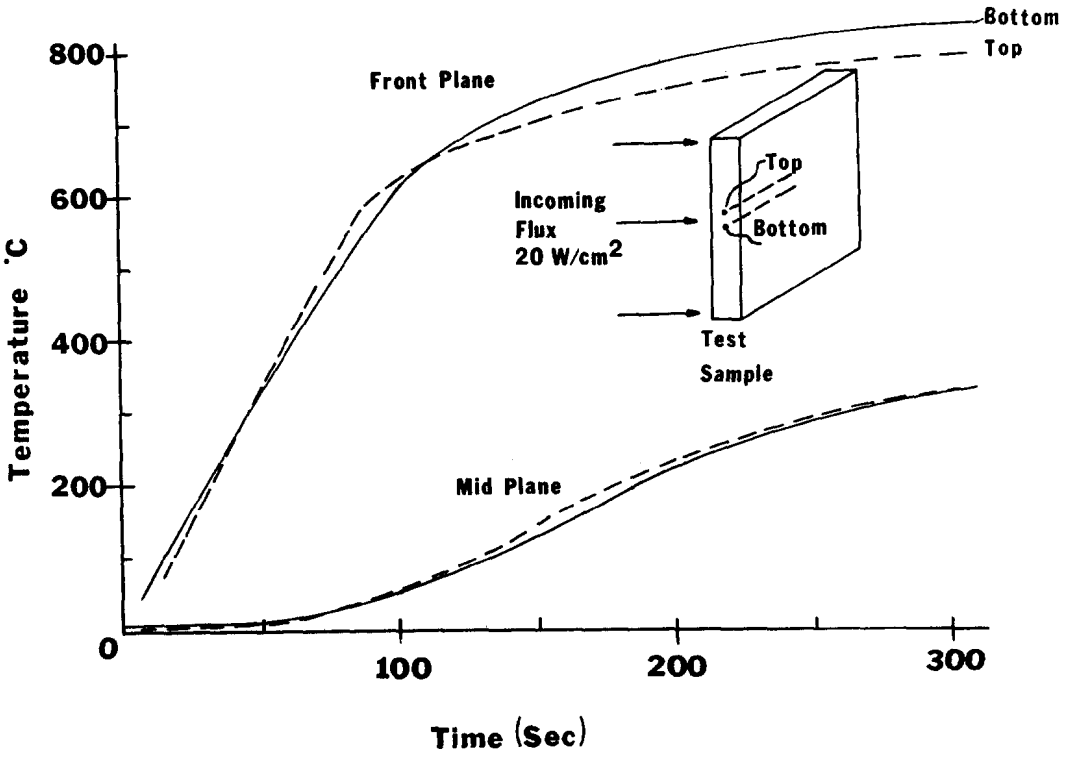

Figure D-1. Thermcouple measurements in the front and mid-plane of the insulation sample to insure uniform incident flux across the sample

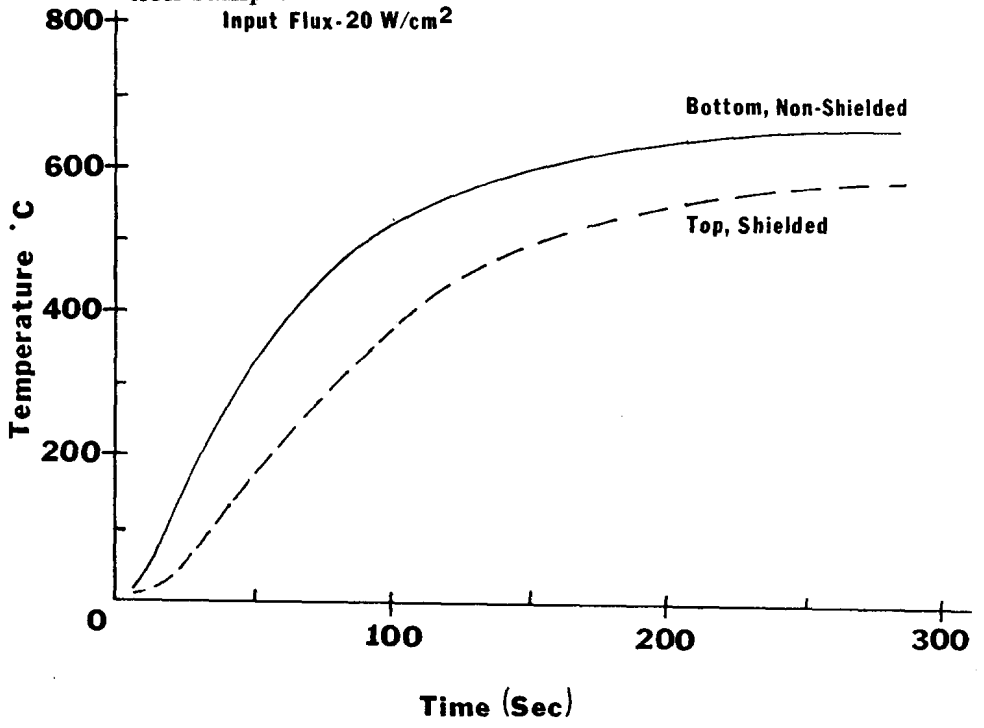

Figure D-2. Measurements showing the effect of shielded vs. unshielded thermocouples in mid-plane of the insulation sample

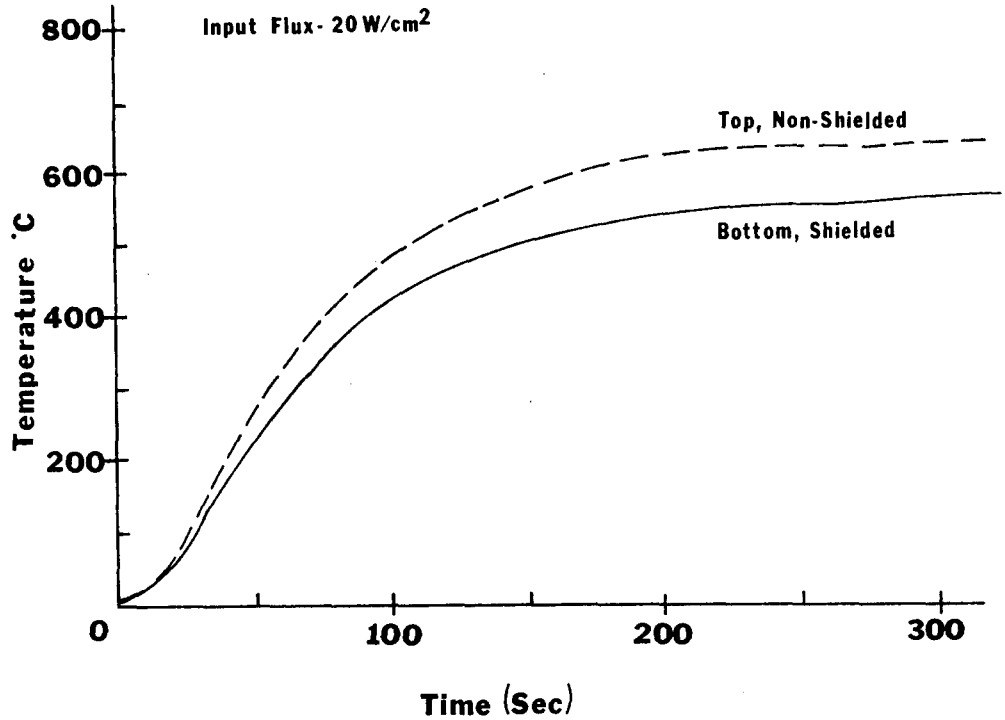

Figure D-3. Shielded vs. unshielded thermocouples, with top and bottom positions reversed from Figure D-2

To measure the effect of shielding the thermocouple, two thermocouples were placed in the appropriate plane of the material such that each thermocouple experience the same heat flux. The incoming flux distribution from the solar furnace was measured to allow the thermocouples to be correctly positioned on the stand. As a second assurance of equal flux on both thermocouples, a short test was performed with two shielded thermocouples. Two shielded thermocouples were placed in each plane (first the middle plane, then the front plane) and a transient heat-up test was performed. If the flux is the same on both thermocouples, the readings will be approximately the same. The flux was deemed uniform when the thermocouples read within 5% of each other. Figure D-1 shows results of this test.

After the materials were correctly positioned in the furnace, measurements with a shielded and a nonshielded thermocouple were made. Figures D-2 and D-3 show results for the middle plane. In Figure D-2 a nonshielded thermocouple was placed above the shielded thermocouple. For comparison, the two thermocouples were switched in Figure D-3. In both cases, the steady state temperature measured by the nonshielded thermocouples was at least 10% greater than the shielded thermocouples. This result is expected, due to the transparent nature of the material. In fact, in over 30 test runs on this material, we found the same result.

Figure D-4 shows the results for the front plane. They are similar (within approximately 10%) to those shown in Figures D-2 and D-3.

Figure D-5 shows the effect of installing the shielded thermocouples from the back. Since the temperature gradient in the sample is from front to back rather than side to side, the preferable thermocouple placement is from the side, along an

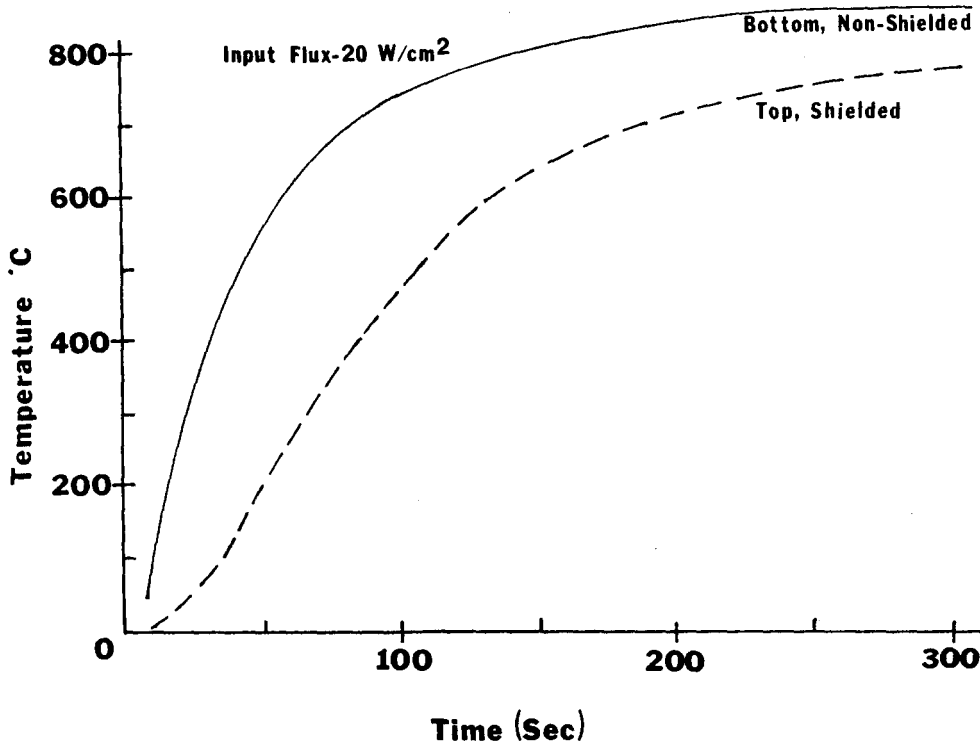

Figure D-4. Shielded vs. unshielded thermocouples in the front plane of the insulation sample

isothermal plane. Conduction losses are greater for the back-installed thermocouple, thereby leading to a lower temperture measurement, compared to the side-installed thermocouple. After several tests, we determined the difference was 10 to 15%. In the MSEE receiver, it was necessary to install the thermocouples from the back because the insulation was already in place in the receiver cavity. Results from Figure D-5 can be used to correct MSEE cavity wall measurements.

Figures D-6 and D-7 show the effect of moving the back-mounted thermocouple 0.4 cm back and forward from its correct position. At an input flux level of 20 W/cm^2 a noticeable difference in measured temperature is seen, due to the high temperature gradient through the material. The calculated temperature distribution shows the same gradient, and therefore the same sensitivity to thermocouple position. However, at lower flux levels gradient is much less, which is helpful since the actual flux levels on the MSEE cavity walls are on the order of 0.1 to 5 W/cm^2. Several tests were executed to statistically determine the effect of temperature gradient on actual vs. expected thermocouple locations. An error we are not able to quantify is that due to changing contact between the thermocouple and insulation if the thermocouple moves.

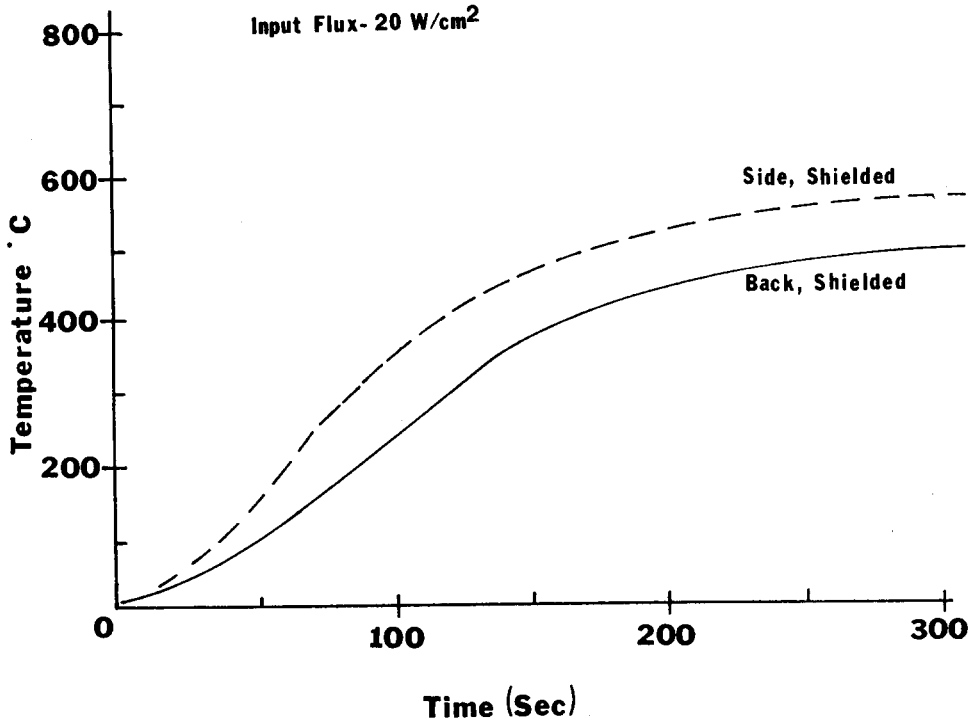

Figure D-5. Measurements showing effect of installing thermcouple along a non-isothermal plane, from the back rather than the side of the insulation sample

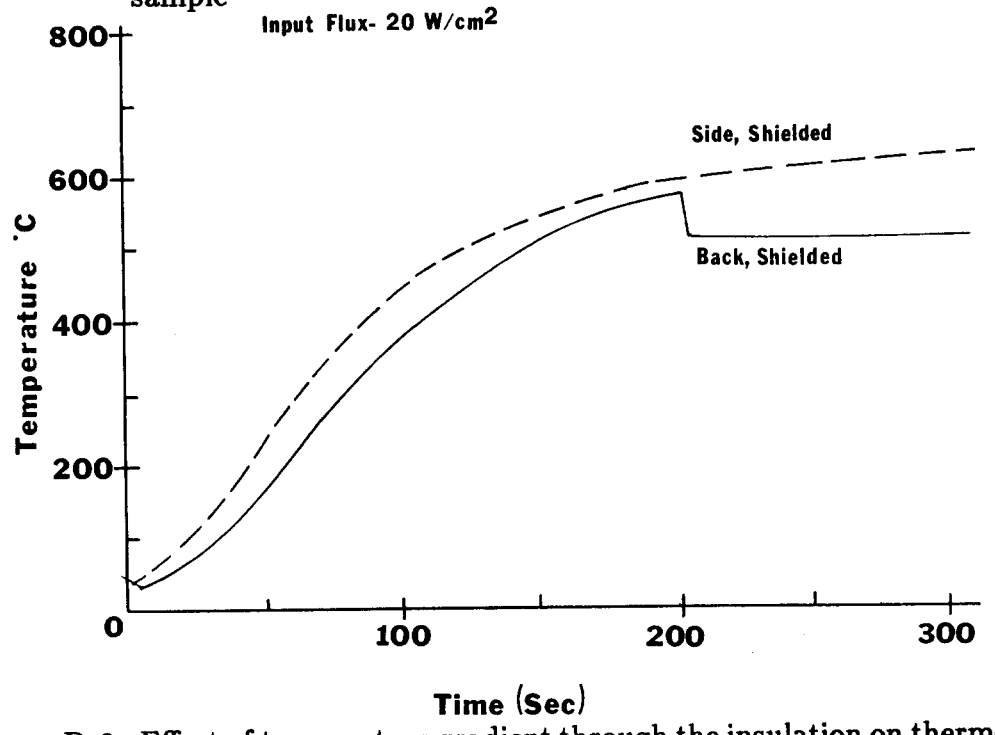

Figure D-6. Effect of temperature gradient through the insulation on thermocouple position. At t = 200 seconds, the thermocouple was pulled back 0.4 cm from its original position

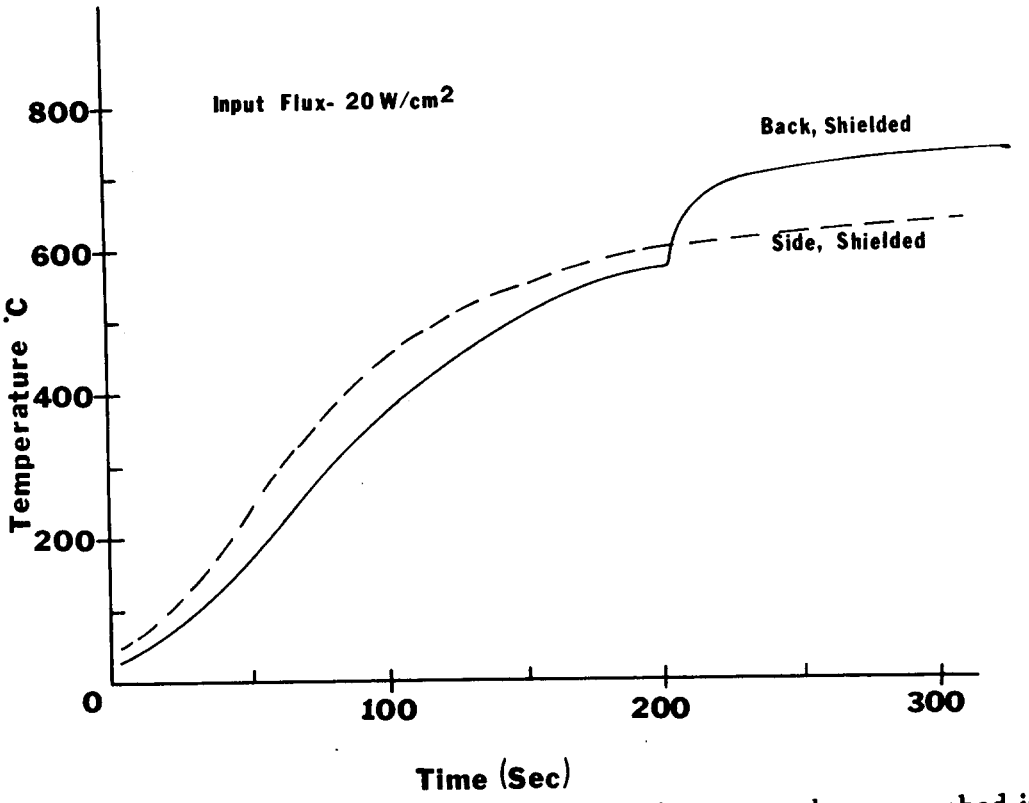

Figure D-7. Thermocouple position effect where thermocouple was pushed in 0.4 cm from its original position

Section 4. Computer Model - Total

The computer model TOTAL[7] calculates the temperature distribution within the insulation, given incident flux as a boundary condition. TOTAL uses the coupled energy equation and the radiative equation of transfer. The equation of transfer was approximated using the modified two-flux equations of Domoto and Wang[8]. Equations D-1 through D-9 represent the differential equations and boundary and initial conditions solved in TOTAL. The program uses the two spectral band approach with the first band making calculations assuming spectral dependence.

$$\rho c \frac{\partial T}{\partial t} = k \frac{\partial^2 T}{\partial x^2} + \left(\frac{dk}{dT}\right)\left(\frac{\partial T}{\partial x}\right)^2 - \frac{dQ}{dx} \qquad (D-1)$$

The boundary and initial conditions are:

$$0 = k \frac{\partial T(x,t)}{\partial x}|_{x=0} - h(T(0,t) - T_\infty) + \int_{\lambda_c}^{\lambda_\infty} \alpha_\lambda G_\lambda d\lambda - \int_{\lambda_c}^{\lambda_\infty} \epsilon_\lambda E_{b\lambda} d\lambda \qquad (D-2)$$

$$0 = -k \frac{\partial T(x,t)}{\partial x}|_{x=x_1} - h(T(x_1,t) - T_\infty) - \int_{\lambda_c}^{\lambda_\infty} \epsilon_\lambda E_{b\lambda} d\lambda \qquad (D-3)$$

and

$$T(x,0) = T_\infty \qquad (D-4)$$

$$\mu \frac{\partial I_\lambda}{\partial x} = -K_\lambda I_\lambda + a_\lambda n_\lambda^2 I_{\lambda b} + \frac{\sigma_\lambda}{4\pi} \int_{\mu'} \int_{\phi'} I_\lambda(x, \mu', \phi') \phi_\lambda(\mu', \phi', \mu, \phi) d\mu' d\phi' \qquad (D-5)$$

$$\frac{dq_\lambda^+(t)}{dt} = -\sqrt{3}(1 - (1-b)\Omega_{o\lambda}) q_\lambda^+(t) + \sqrt{3}\Omega_{o\lambda} b q_\lambda^-(t) + \sqrt{3}(1 - \Omega_{o\lambda}) n_\lambda^2 E_{b\lambda}(T) \qquad (D-6)$$

$$-\frac{dq_\lambda^-(t)}{dt} = -\sqrt{3}(1 - (1-b)\Omega_{o\lambda}) q_\lambda^-(t) + \sqrt{3}\Omega_{o\lambda} b q_\lambda^+(t) + \sqrt{3}(1 - \Omega_{o\lambda}) n_\lambda^2 E_{b\lambda}(T) \qquad (D-7)$$

The boundary conditions are,

$$q_\lambda^+(0) = (1 - \rho_{o\lambda})F_\lambda(0) + \rho_{i\lambda}q_\lambda^-(0) \qquad (D-8)$$

$$q_\lambda^-(\ell) = \rho_{i\lambda}q_\lambda^+(\ell) \qquad (D-9)$$

Table D–1 shows the steady state temperature distribution as calculated from TOTAL and the two measurements made in the NMSU solar furnace. TOTAL was not adjusted to fit the measurements. Material property data from the manufacturer was placed directly into the program. Parameters describing the radiation transfer through the alumina-silica insulation were not available. Estimates from past experience with zirchonia insulation were used. Nontheless, the calculations compare very well with the front plane temperature measurements. The comparison is not as good with the mid-plane measurements. However, for the MSEE cavity wall we are most interested in front surface temperatures.

Section 5. MSEE Measurements and Comparisons

The measurements taken at the NMSU solar furnace were made with an incident solar flux of 20 W/cm^2. Actual temperature measurements inside of the reeiver were takin in regions of much lower flux levels, therefore thermocouple placement was not as critical as it was for the higher flux levels at NMSU solar furnace. Table D–2 shows calculations and measurements compare within the accuracy of the flux estimates, about $\pm 10\%$.

TABLE D-1
TEMPERATURE GRADIENT THROUGH INSULATIN SAMPLE AT NMSU SOLAR FURNACE AS PREDICTED BY COMPUTER MODEL TOTAL, AND AS MEASURED BY SHIELDED THERMOCOUPLES IMBEDDED IN SAMPLE. INCIDENT FLUX IS 20 W/CM^2

Location from front surface (cm)	Calculations (K)	Measurements (K)
0	1035	
0.203	1170	
0.406	1155	
0.610	1130	1120
0.813	1100	
1.016	1060	
1.219	1025	900
1.422	980	
1.626	935	
1.829	880	
2.032	810	
2.235	725	
2.540	510	

TABLE D-2
TOTAL COMPUTER MODEL PREDICTS TEMPERATURES ON MSEE CAVITY WALLS WITHIN 10% OF THERMOCOUPLE MEASUREMENTS. INCIDENT FLUX USED AS BOUNDARY CONDITION IN TOTAL IS ESTIMATED FROM HELIOS COMPUTER CODE

Location in Cavity	Flux (W/cm^2)	Measured Temperature (K)	Calculated Temperature (K)
East Wall	1.1	505	480
West Wall	0.9	510	475
Bottom	2.5	560	610

Section 6. Conclusions

Several conclusions can be made from this study.

1. Unshielded thermocouples consistently read 10% higher than shielded thermocouples. Therefore shielded thermocouples should always be used when measuring the temperature of alumina-silica insulation.
2. Thermocouple placement is more important in high flux areas than in low flux areas.
3. More temperature and flux measurements inside receiver cavities is warranted with an emphasis on better placement of the transducers.
4. Accuracy better than $\pm 10\%$ will be difficult to attain given the nature of the material and environment.
5. More detailed modeling of the cavity is warranted, being sure to consider the semitransparent nature of the insulating material.

In general, reasonable temperature measurements and calculations ($\pm 10\%$) can be achieved in a solar receiver such as the MSEE solar receiver, however, care must be taken to use the thermocouples and interpret the data correctly.

APPENDIX D REFERENCES

1. Matthews, L. K., and Mulholland, G. P., "High Temperature - High Flux Material Testing for Solar Flux Applications," Solar Energy 21, 175-181 (1979).
2. Matthews, L. K., "Theoretical and Experimental Investigation of High Temperature Insulators Subjected to Intense Visible Radiation," AIAA 21st. Aerospace Sciences Meeting, paper number AIAA-83-0158 (1983).
3. Matthews, L. K., and Viskanta, R., and Incropera, F. P., "Development of Inverse Methods for Determining Thermophysical and Radiative Properties of High Temperature Fibrous Materials," International Journal of Heat and Mass Transfer, Vol 27(4), 487-495 (1984).
4. Matthews, L. K., and Viskanta, R., and Incropera, F. P., "Combined Conduction and Radiation Heat Transfer in Pourous Materials Heated by Intense Solar Radiation," ASME Journal of Solar Engineering, Vol. 107, 29-34 (1985).
5. MSEE Phase I report by Martin Marietta prepared by Sandia National Laboratories, Livermore California, Sandia Report number SAND 85-8175.
6. Clark, R., and Matthews, L. K., and Mulholland, G. P., "The NMSU Solar Furnace Facility," Alternative Sources III, Solar Energy, Vol. 3, 33-48 (1980), 3rd Miami International Conference on Alternative Energy Sources.
7. Matthews, L. K., "Experimental and Theoretical Analysis of the High Flux - High Temperature Field in a Dielectric Subjected to Intense Solar Radiation," Ph.D Thesis, Purdue University, 1982, DAI# 43/12B, p. 4108, UMI# PSH83-10769.
8. Domoto, G. A., and Wang, W., "Radiative Transfer in Homogenous Nongray Gases with Nonisotropic Particle Scattering," ASME Journal of Heat Transfer, vol. 96, 385-390 (1974).

UNLIMITED RELEASE
INITIAL DISTRIBUTION

U.S. Department of Energy (5)
Forrestal Building
Code CE-314
1000 Independence Avenue, S.W.
Washington, D.C. 20585
Attn: H. S. Coleman
S. Gronich
F. H. Morse
M. R. Scheve
R. Shivers

U.S. Department of Energy
Forrestal Building, Room 5H021C
Code CE-33
1000 Independence Avenue, S.W.
Washington, D.C. 20585
Attn: C. Carwile

U. S. Department of Energy
P.O. Box 5400
Albuquerque, NM 87115
Attn: D. Graves

U.S. Department of Energy
1333 Broadway
Oakland, CA 94612
Attn: R. Hughey

University of California
Environmental Science and Engineering
Los Angeles, CA 90024
Attn: R. G. Lindberg

University of Houston (2)
Solar Energy Laboratory
4800 Calhoun
Houston, TX 77704
Attn: A. F. Hildebrandt
L. Vant-Hull

University of Kentucky
Dept. of Chemical Engineering
Lexington, KY 40506
Attn: J. E. Funk

University of Utah
Mechanical & Ind. Engineering Dept.
Salt Lake City, Utah 84112
Attn: R. F. Boehm

Analysis Review & Critique
6503 81st Street
Cabin John, MD 20818
Attn: C. La Porta

Arizona Public Service Company
P.O. Box 21666
Phoenix, AZ 85036
Attn: E. Weber

Babcock and Wilcox
91 Stirling Avenue
Barberton, OH 44203
Attn: D. Young

Bechtel Group, Inc.
P. O. Box 3965
San Francisco, CA 94119
Attn: P. DeLaquil
S. Fleming

Black & Veatch Consulting Engineers (2)
P.O. Box 8405
Kansas City, MO 64114
Attn: J. C. Grosskreutz
J. E. Harder

Boeing Aerospace
Mailstop JA-83
P. O. Box 1470
Huntsville, AL 35807
Attn: W. D. Beverly

California Energy Commission
1516 Ninth St., M/S 40
Sacramento, CA 95814
Attn: A. Jenkins

California Public Utilities Com.
Resource Branch, Room 5198
455 Golden Gate Ave.
San Francisco, CA 94102
Attn: T. Thompson

Centro Investigations Energetica
Medroansental Technologie (CIEMAT)
Avda. Complutense, 22
28040 Madrid
Spain
Attn: F. Sanchez

DFVLR EN-TT
Institute for Technical Thermodynamics
Pfaffenwaldring 38-40
7000 Stuttgart 80
Federal Republic of Germany
Attn: Dr. Rainer Koehne

El Paso Electric Company
P.O. Box 982
El Paso, TX 79946
Attn: J. E. Brown

Electric Power Research Institute (2)
P.O. Box 10412
Palo Alto, CA 94303
Attn: J. Bigger
E. DeMeo

Foster Wheeler Solar Development Corp.
12 Peach Tree Hill Road
Livingston, NJ 07039
Attn: S. F. Wu

Georgia Institute of Technology
Engineering Experiment Street
Atlanta, GA 30332
Attn: C. T. Brown

Jet Propulsion Laboratory
4800 Oak Grove Drive
Pasadena, CA 91103
Attn: M. Alper

Los Angeles Department of Water and Power
Alternate Energy Systems
Room 661A
111 North Hope St.
Los Angeles, CA 90012
Attn: Hung Ben Chu

Martin Marietta Aerospace
P.O. Box 179, MS L0450
Denver, CO 80201
Attn: H. Wroton

McDonnell Douglas (4)
MS 49-2
5301 Bolsa Avenue
Huntington Beach, CA 92647
Attn: D. Barron
R. L. Gervais
J. E. Raetz
S. Saloff

Meridian Corporation
5113 Leesburg Pike
Falls Church, VA 22041
Attn: D. Kumar

Olin Chemicals Group (2)
120 Long Ridge Road
Stamford, CT 06904
Attn: F. N. Christopher
D. A. Csejka

Pacific Gas and Electric Company
77 Beale Street
San Francisco, CA 94106
Attn: J. Laszlo

Pacific Gas and Electric Company (4)
3400 Crow Canyon Road
San Ramon, CA 94526
Attn: G. Braun
T. Hillesland, Jr.
B. Norris
C. Weinberg

Rockwell International
Rocketdyne Division
6633 Canoga Avenue
Canoga Park, CA 91304
Attn: J. Friefeld

Sandia Solar One Office
P.O. Box 366
Daggett, CA 92327
Attn: A. Snedeker

Science Applications International Corp.
10401 Roselle Street
San Diego, CA 92121
Attn: B. Butler

Solar Energy Research Institute (2)
1617 Cole Boulevard
Golden, CO 80401
Attn: B. Gupta
D. Hawkins

Solar Kinetics Inc. (2)
P.O. Box 47045
Dallas, TX 75247
Attn: J. A. Hutchison
D. L. White

Southern California Edison
P.O. Box 325
Daggett, CA 92327
Attn: C. Lopez

Southern California Edison (31)
P.O. Box 800
Rosemead, CA 92807
Attn: J. N. Reeves
P. Skvarna (30)

Stearns Catalytic Corp.
P.O. Box 5888
Denver, CO 80217
Attn: T. E. Olson

Stone and Webster Engineering Corporation
P.O. Box 1214
Boston, MA 02107
Attn: R. W. Kuhr

6000	E. H. Beckner; Attn:	V. Dugan, 6200
6220	D. G. Schueler	
6222	K. R. Boldt	
6222	W. A. Couch	
6222	C. Maxwell	
6222	J. V. Otts	
6226	J. M. Chavez	
6226	J. T. Holmes (10)	
6226	C. E. Tyner	
8000	R. S. Claassen; Attn:	E. E. Ives, 8100
		R. J. Detry, 8200
		P. Mattern, 8300

8131 S. E. Faas
8152 J. C. Swearengen
8241 D. B. Dawson
8241 W. R. Delameter
8244 C. Hartwig
8245 R. J. Kee
8400 R. C. Wayne; Attn: R. C. Wayne (acting), 8430
H. Hanser, 8440
8434 M. C. Stoddard
8470 R. L. Rinne
8471 A. F. Baker
8471 N. E. Bergan (5)
8471 P. K. Falcone
8471 B. L. Kistler
8471 A. C. Skinrood (3)
8471 D. N. Tanner
8265 Publications Division for OSTI (30)
8265 Publications/Technical Library Processes, 3141
3141 Technical Library Processes Division, (3)
8024 Central Technical Files (3)